Die approbierte Originalversion dieser Diplom-/Masterarbeit ist an der Hauptbibliothek der Technischen Universität Wien aufgestellt (http://www.ub.tuwien.ac.at).

The approved original version of this diploma or master thesis is available at the main library of the Vienna University of Technology (http://www.ub.tuwien.ac.at/englweb/).

TECHNISCHE UNIVERSITÄT WIEN

VIENNA UNIVERSITY OF TECHNOLOGY

DIPLOMARBEIT

Simulation of the Excitation of Human Lower Spinal Cord Structures with Surface Electrodes: 3D Finite Element Analysis and Nerve Fiber Modeling

Ausgeführt am Institut für

ANALYSIS UND SCIENTIFIC COMPUTING

DER TECHNISCHEN UNIVERSITÄT WIEN

unter der Anleitung von

Ao.Univ.Prof. DI DDDr. Frank Rattay

und

DI Dr. Karen Minassian

durch

Josef Ladenbauer

Hahngasse 15/21

1090, Wien

Wien, im Oktober 2008

Acknowledgements

I thank Prof. Frank Rattay[1] and Dr. Karen Minassian[1,2] for scientific support and helpful extensive discussions. Thanks to DI Zoltan Szava for support in FEM modeling matters.
Special thanks to my parents, DI Irene Hofstetter and Sarah Wulfert for last-minute proof-reading and constructive comments.
Gratitude is extended to all my friends who inspired and motivated me in various ways throughout my study.

[1]Institute for Analysis and Scientific Computing, Vienna University of Technology
[2]Center of Biomedical Engineering and Physics, Medical University of Vienna

Abstract

A new stimulation method utilizing surface electrodes is efficient in exciting spinal cord neurons similarly as with implanted electrodes that are surgically placed close to the neural target structures. This result is promising to become of great importance for paralyzed people because with this non-invasive method some inherent functions of the spinal cord controlling stepping and standing can be activated.

The biophysical and neuro-physiological processes in electrical stimulation of the lower spinal cord are simulated using mathematical tools. First the electric field generated by the electrodes is computed. The Laplace equation is solved to obtain the electrical potentials determined by the geometry of the various anatomical structures and their electrical conductivities. A numerical technique, the finite element method, is applied to calculate the steady-state solution of this three-dimensional problem with appropriate boundary conditions. In the following step the calculated electrical potentials are evaluated along the pathways of representative spinal cord nerve fibers. These voltage profiles are the imposed extracellular potentials of the fibers and serve as input data for a nerve fiber model. Response behavior and excitation thresholds of the fibers are computed with this model.
The excitation patterns of target neurons stimulated with surface electrodes and implants are analyzed. Factors influencing the excitability of the nerves like distance to the electrodes and different stimulation signals are studied, and the relationship between stimulus strength and the excitation order of different nerve fibers is investigated.

Activation of neural structures in the lower spinal cord using surface electrodes is feasible. Direct results of the simulations inform about the excitability of the studied nerve structures and demonstrate a definite relation between stimulus strength and the excitation order of nerve fibers coming from different regions. Comparison with simulation results involving an implanted electrode reveals similarities in the excitation patterns of the same target neurons in both stimulation techniques.
The simulation results provide a biophysical explanation for the clinical observation of muscle responses in the lower limbs induced by spinal cord stimulation from the surface. Furthermore, with appropriate positions for surface and implanted electrodes a comparable neural input for the central pattern generators for locomotion within the spinal cord is obtained. Thus, similar effects can be achieved in both stimulation strategies.

Kurzfassung

Die Anwendung von Oberflächenelektroden ist eine effiziente Methode zur Stimulation von Nervenstrukturen im menschlichen Rückenmark. Die Wirkung ist vergleichbar mit jener von implantierten Elektroden, welche operativ in der Nähe des Rückenmarks platziert werden. Dieses Ergebnis ist vielversprechend für Gelähmte, da durch diese neue nicht-invasive Methode neuronale Netzwerke im Rückenmark, welche das Stehen und Gehen kontrollieren, einfacher aktiviert werden können.

Mittels Anwendung mathematischer Werkzeuge wurden die biophysikalischen und neurophysiologischen Vorgänge bei der elektrischen Stimulation des unteren Rückenmarks simuliert. Zunächst wurde das durch die Elektroden generierte elektrische Feld berechnet. Dazu wurde die Laplacegleichung für das dreidimensionale stationäre elektrische Strömungsfeld im komplexen System des Rückenmarks und der umliegenden Schichten gelöst. Das entsprechende Randwertproblem wurde mithilfe der Finiten-Elemente-Methode behandelt. Im darauffolgenden Schritt wurde die errechnete Potentialverteilung auf die Trajektorien repräsentativer Rückenmarksnerven abgebildet um die künstlich hervorgerufenen extrazellulären Potentiale entlang der Targetneuronen zu erhalten. Diese dienten als Eingangsdaten für ein Nervenfaser-Modell, mit dem die Reaktionen und Anregungsschwellen der verschiedenen Rückenmarksnerven analysiert wurden.

Neurale Strukturen im unteren Rückenmark können mit Oberflächenelektroden aktiviert werden. Die Resultate der Simulationen geben Aufschluss über die Anregbarkeit verschiedener Nervenstrukturen des Rückenmarks und zeigen einen direkten Zusammenhang zwischen Stimulationsstärke und Anregungsreihenfolge der simulierten Nerven. Der Vergleich mit den Ergebnissen von Simulationen mit implantierten Elektroden lässt Ähnlichkeiten in den Erregungsmustern von Fasern in beiden Stimulationstechniken erkennen.
Die Berechnungen liefern eine biophysikalische Erklärung für die klinische Beobachtung von Muskelzuckungen in den unteren Extremitäten, ausgelöst durch Rückenmarkstimulation mittels Oberflächenelektroden. Weiters kann mit passenden Elektrodenpositionen ein vergleichbarer neuraler Input für die „Mustergeneratoren“ für Fortbewegung im Rückenmark erreicht werden. Somit werden mit beiden Stimulationsstrategien ähnliche Effekte erzielt.

Glossary

Action potential (AP, spike) – Electrical signal transmitted through neurons, fundamental unit of information in the nervous system

Axon – Long projection of a neuron, that conducts action potentials away from the cell body of the neuron

Dorsal column (DC) fiber – Longitudinal fibers located in the white matter of the spinal cord

Dorsal root (DR) fiber – Nerve fibers entering the spinal cord

Dura mater – Cerebral membrane surrounding the spinal cord

Epidural – Outside the dura mater within the spinal canal

Nerve fiber – Axon including myelin sheath

Spinal canal – Bony canal formed by the spinal column where the spinal cord is located

Spinal cord – Elongated, approximately cylindrical part of the central nervous system enclosed in the spine

Spinal cord stimulation (SCS) – Stimulation of spinal cord neurons with electrodes

Spinal roots – Initial segments of the nerves entering (dorsally) or exiting (ventrally) the spinal cord

Spine, spinal column – Backbone, row of bones along the back

Transcutaneous – Through the skin

Ventral root (VR) fiber – Nerve fibers exiting from the spinal cord

Vertebra – Any one of the spinal column segments

Contents

Acknowledgements i
Abstract ii
Kurzfassung iii
Glossary iv

1. Introduction **1**

2. Anatomical and Physiological Background **4**
2.1. The Neuron and Action Potentials 4
2.2. Extracellular Stimulation of Nervous Tissue 6
2.3. Anatomy of Spinal Cord and Spine 8
2.4. Relation Between Excited Spinal Root Fibers and Corresponding Muscle Responses 10
2.5. Geometry of Spinal Root Fibers and Dorsal Column Fibers 12

3. Volume Conductor Model **15**
3.1. Problem Formulation 15
3.2. Numerical Methods 17
3.3. Implementation of the Model 20
3.3.1. Model Geometry 20
3.3.2. Tissue Conductivities 22
3.3.3. Boundary Conditions 24
3.3.4. Solution of the VC Problem 25

4. Nerve Fiber Model **26**
4.1. Activating Function 29
4.2. Membrane Equations 30
4.3. Parameter Values 32

5. Results **33**
5.1. Standard Geometry of Simulated Root Fibers 33
5.2. Extracellular Voltage Profiles and Excitation Thresholds of Spinal Root Fibers 36
5.3. Modifications of the VC Model Geometry - Effects on Extracellular Voltage and Excitation Thresholds of Spinal Root Fibers 42
5.3.1. VC Model Extension 43
5.3.2. VC Model including Liver 45
5.3.3. VC Model including Aorta 46
5.4. Comparison with Simulations of Neural Responses using an Implanted Electrode 49
5.4.1. Implementation of an Implanted Electrode in the VC Model . . 49
5.4.2. Surface Electrodes (tSCS) versus Implant (eSCS) - Comparison of Spinal Root Fiber Excitation 51

6. Discussion **59**
6.1. Similarities of Neural Responses in tSCS and eSCS 59
6.2. Relationship between Stimulus Strength and Muscle Response 61
6.3. Factors Limiting the Accuracy of the Simulations 63
6.3.1. Skin Capacitance 63
6.3.2. Rheobase and Chronaxie 64
6.3.3. Node Positions 65
6.3.4. VC Model Geometry 66

7. Conclusion **67**

A. Appendix **69**
A.1. MATLAB Code 69

Bibliography **75**

1. Introduction

Electrical stimulation of lower spinal cord neurons is one of the most promising approaches to improve motor function in spinal cord injured patients with paralyzed limbs. It has been shown that spinal cord stimulation with electrodes implanted in the epidural space (inside the vertebral canal but outside of the spinal cord) can evoke rhythmical, stepping-like movements in the paralyzed lower limbs of individuals with complete spinal cord injury [Dimitrijevic et al. 1998, Minassian et al. 2007b]. Thus direct evidence for a human spinal locomotor pattern generator was provided. Using this stimulation technique, the directly electrically activated neural structures were identified to be large-diameter afferent neurons entering the back side of the spinal cord through the so called dorsal roots, mediating the generated input to the spinal locomotor centers [Murg et al. 2000, Minassian et al. 2000, Holsheimer 1998].

Computational studies have shown that dorsal root activation is not principally determined by a focal stimulation, but rather by the anatomy of the nerve fiber, i.e. fiber diameter, location and curvature [Struijk et al. 1993a, Rattay et al. 2000]. Recent studies have demonstrated that dorsal spinal cord structures can also be excited utilizing surface electrodes attached at the back and abdomen and applying moderate stimulus intensities [Minassian et al. 2007a, Hofstoetter et al. 2008]. This can be explained by the geometry of the vertebral column. Anatomical structures with low electrical resistivity between neighboring vertebrae allow current to flow into the vertebral canal.

Stimulation from the surface involves electrodes which are applied on the skin and can easily be removed after the session. With this non-invasive method, neither biocompatibility nor infection problems can arise. Spinal cord stimulation with implanted electrodes is effective but cost-intensive since it requires a surgical procedure, and its efficacy depends on aftercare for a prolonged period of time.

Several modeling studies of spinal cord stimulation (SCS) with implanted electrodes have appeared in literature [Holsheimer 1998], however the effects of utilizing surface electrodes in SCS have not been simulated.

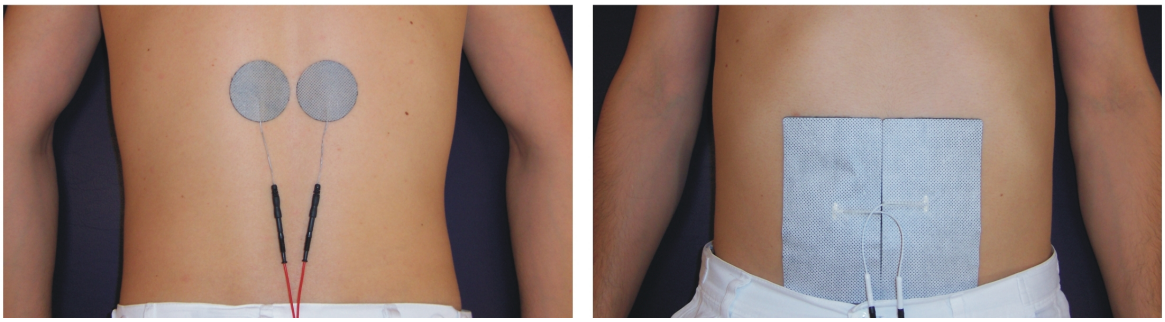

Figure 1.1.: Placement of the stimulating electrodes on the back (left) and the indifferent electrodes on the abdomen (right). The two electrodes of each pair are connected to function as a single electrode.

The aim of this thesis is to gain a better insight into the immediate effects of SCS from the surface through computer simulation and to provide a contribution to the optimization of the stimulation technique for controlled dorsal root stimulation.

The stimulation-evoked electrical phenomena include two main aspects. First, the potential difference between the electrodes during a stimulation pulse causes ionic current to flow through the intermediate anatomical structures: the volume conductor. A potential distribution is generated, determined by the geometrical relations and electrical properties of the anatomical structures. Secondly, the electrical field causes local depolarization or hyperpolarization of nerve cell membranes. If a nerve fiber membrane is sufficiently depolarized, an action potential will be initiated. These two separate aspects can be represented by a volume conductor model and a nerve fiber model, respectively.

In Chapter 3 the finite element method is applied using the commercially available software COMSOL Multiphysics (former FEMLAB) to calculate the solution of the differential equations describing the three-dimensional potential distribution and current density generated by the electrical stimulation within the volume conductor model. Quasi-stationary conditions are assumed, i.e. capacitive effects between the electrodes and the biological materials are neglected when the electric field is computed. The inhomogeneous and anisotropic solution domain is represented by a three-dimensional model of anatomical structures relevant to the simulation including: white and gray matter of the spinal cord, cerebrospinal fluid, epidural fat, vertebral bones, vertebral discs, paraspinal muscles, a simplified model of the thorax, fat, skin, and two electrode compartments. The vertebral column is constructed with detailed geometry, the other relevant anatomical structures are simulated as prismatic compartments similarly to the modeling study of [Szava 2006]. The studied electrode setups are implemented as

Dirichlet boundary conditions with constant voltages applied at the external surfaces of the electrode compartments.

The calculated electric field is evaluated along the trajectories of representative target neurons (Chapter 4). These voltage profiles are used as input data for a nerve fiber model to simulate the responses of the myelinated nerve fibers to the imposed field. The nonlinear gating mechanism of ion channels in the active parts (nodes of Ranvier) of the target fibers are incorporated using the model of Sweeney et al. [Chiu et al. 1979, Sweeney et al. 1987].

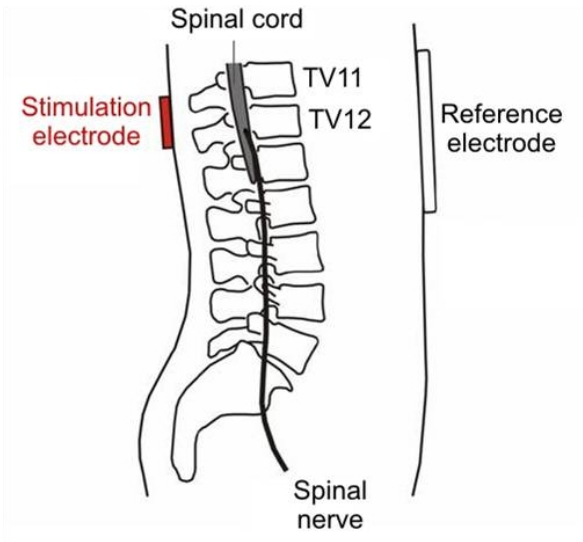

Figure 1.2.: Illustration of SCS with surface electrodes.

The excitability of several dorsal and ventral root fibers, entering the spinal cord and exiting the spinal canal at different levels, is studied (Chapter 5), and the relationship between stimulus strength and the excitation order of different nerve fibers is investigated (Section 6.2). Single stimuli with a pulse width of 1ms are applied in 1V increments, until action potentials are initiated and propagated in the simulated neurons.

To compare the effects of spinal cord stimulation from the surface with the case of using an implant the potential distribution within the volume conductor is calculated again applying the finite element method, representing the electric field generated by an implanted electrode (Sections 5.4 and 6.1). The excitation patterns of the different nerve fibers stimulated with surface and implanted electrodes respectively, are analyzed.

2. Anatomical and Physiological Background

In this study complex neurophysiological processes are simulated using mathematical tools. The quality of the computations depends on accurate anatomical and physiological information. For the volume conductor model a simplified geometry of the relevant anatomical structures has to be defined. The calculated electrical potential distribution within this solution domain is evaluated along the pathways of target neurons and subsequently used as input data for the nerve fiber model. Therefore the excitability of a neuron strongly depends on its geometry. In additon, the fiber diameter and the model used to simulate the ion channel dynamics are important factors influencing the results. Anatomical and physiological knowledge is beneficial for the interpretations of the computed results.

2.1. The Neuron and Action Potentials

Neurons are the main signaling components of the nervous system. The fundamental unit of information processed and transmitted through neurons is an electrical signal called action potential (AP). A typical neuron consists of four main parts: the cell body (soma), the dendrites, the axon, and presynaptic terminals (Figure 2.1). The soma is the metabolic center of the cell, giving rise to two kinds of processes: several short dendrites and one long axon. Dendrites branch out in tree-like fashion and are the main apparatus for receiving incoming APs from other nerve cells. In contrast, the axon extends away from the cell body and is the main conducting unit for carrying APs to other neurons or muscle cells. It is made up of a membrane tube filled with axoplasm.

To increase the speed by which APs are conducted, large axons are wrapped in a fatty, insulating sheath of myelin. This sheath is interrupted at regular intervals by the nodes of Ranvier. These gaps cause a regeneration of the AP. At the end region of an axon neural information is passed on to postsynaptic cells via the release of chemical substances at the presynaptical terminals.

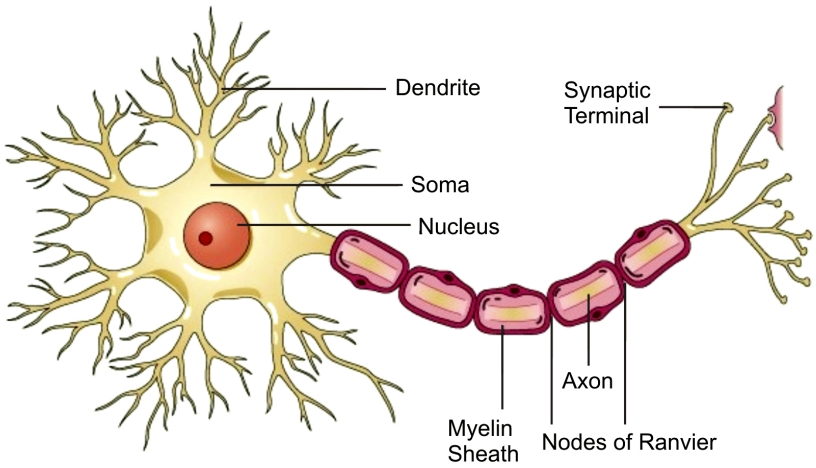

Figure 2.1.: Illustration of a neuron.

The prominent structure that allows nerve fibers to transmit APs is the cellular membrane [Kandel et al. 2000]. It consists of a lipid bilayer, which contains large protein molecules. Some of these protein molecules are ion channels, through which the membrane selectively regulates the chemical exchange of certain ions between the cell and its surrounding. These ion channels are essential for the generation of APs.
Different ionic concentrations in the intracellular and extracellular fluids cause a voltage gradient across the membrane (Figure 2.2). At rest, the inside potential is about 70mV lower than the outside. The cell is in a polarized state. When an axon is depolarized above the threshold of about -55mV (from the resting potential of -70mV) an AP is generated (Figure 2.3) [Kandel et al. 2000].

APs are all-or-none impulses with an amplitude of about 100mV and a duration of about 1ms, traveling along the entire length of a neuron. The speed of the AP propagating along the axon can be in the range of 1 - 100 m/s. Depolarization of the axon below the threshold does not generate an AP and the membrane potential of the axon will return to the resting state.

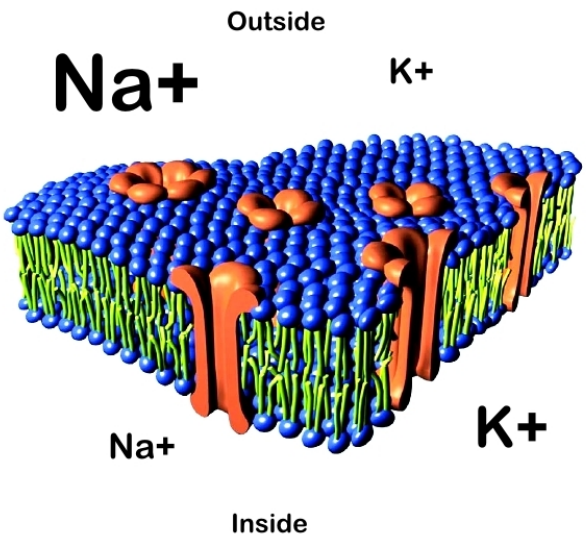

Figure 2.2.: Cell membrane and relation of ion concentrations.

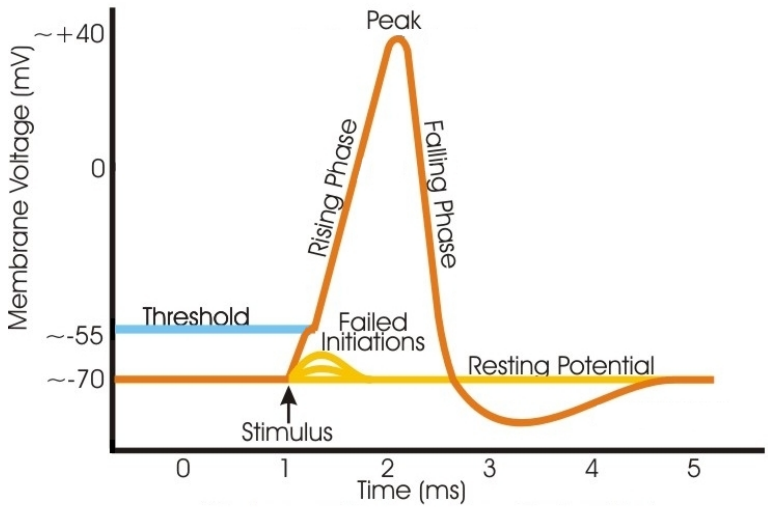

Figure 2.3.: Schematic action potential.

2.2. Extracellular Stimulation of Nervous Tissue

As described in the previous section, APs in neurons are generated by electro-chemical reactions in the brain or the spinal cord. However, it is also possible to artificially excite neurons with electrical currents that are applied to the human body. In tSCS electrodes are placed on the skin and an electrical current pulse is applied. These pulses have a certain amplitude, duration, and repetition frequency. The applied pulse in-

fluences the membrane potential of neurons. Close to the cathode neuronal membrane is depolarized, close to the anode it is hyperpolarized. If the depolarization is large enough (above threshold) an AP is generated. Hyperpolarization drives the membrane potential to lower values (< -70mV) and suppresses the generation of APs [Kandel et al. 2000]. However, when the stimulation current is switched off the membrane potential returns to its resting state, and such a relative depolarization can generate an AP if the hyperpolarization was large enough. In most cases stimulation with positive currents (anodic) needs stronger signals [Rattay 1998]. Positive and negative threshold currents essentially depend on the position and orientation of the neurons relative to the applied electric field. The most excitable part of a neuron is its axon [Rattay 1999].

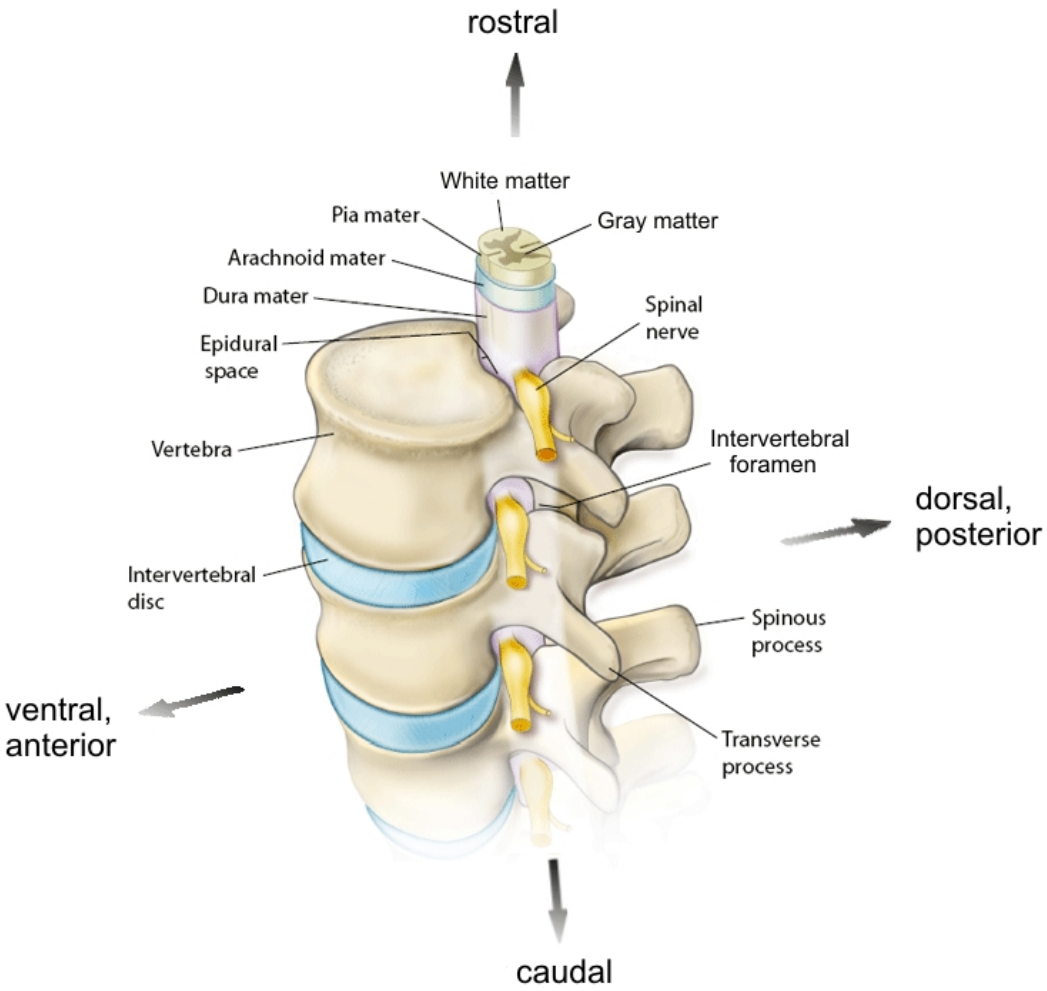

Figure 2.4.: Spinal cord within vertebral column.

2.3. Anatomy of Spinal Cord and Spine

The spinal cord is a long, thin, approximately cylindrical extension of the central nervous system from the brain and is enclosed in and protected by the bony vertebral column (spine). In transverse sections the spinal cord reveals a central H-shaped gray area surrounded by white matter (Figures 2.4, 2.5). The white matter is made up of longitudinally arranged myelinated and unmyelinated nerve fibers. The gray matter contains a continuous matrix of nerve fibers and neuronal cell bodies.
Nerve fibers enter and exit from the spinal cord through the spinal nerve roots. Smaller rootlets unite and form these roots, which leave the spinal cord dorsolaterally and ventrolaterally (Figure 2.5). The dorsal roots carry sensory information into the spinal cord from muscles and skin. In contrast, the ventral roots are bundles of the outgoing axons of motor neurons that innervate muscles.

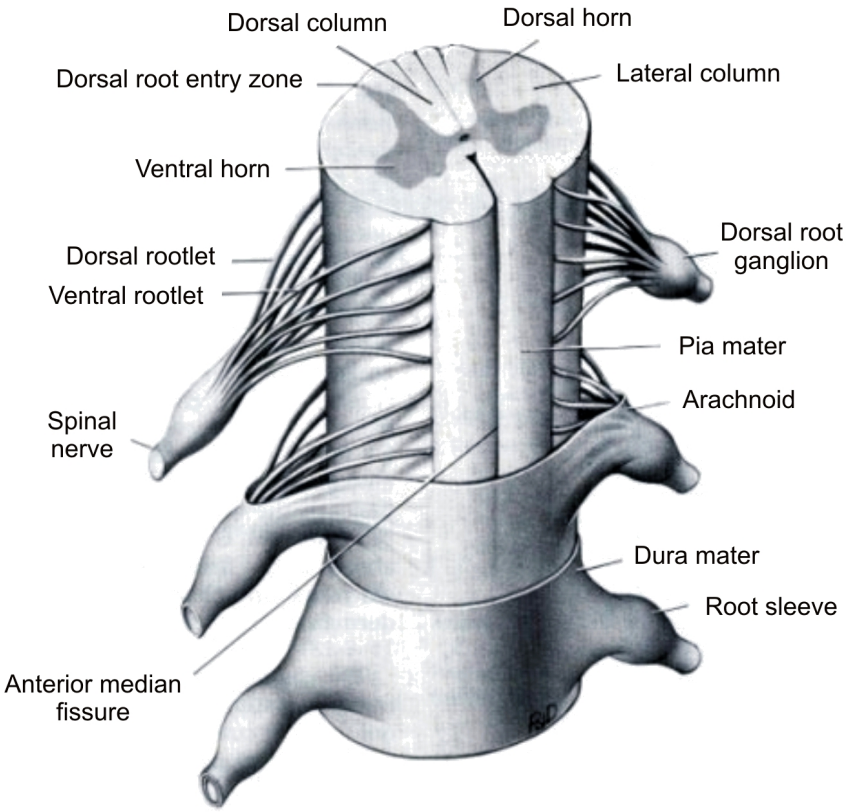

Figure 2.5.: Spinal cord & spinal roots.

The spine supports the spinal cord and is composed of bones called vertebrae, intervertebral discs, and the coccyx (tailbone). Individual vertebrae are named according to region and position, from superior to inferior. Seven cervical vertebrae in the neck (C1-C7) are followed by twelve thoracic vertebrae in the chest (T1-T12), where the ribs attach, five lumbar vertebrae in the lower back (L1-L5) with large bodies, and five fused sacral vertebrae (S1-S5).

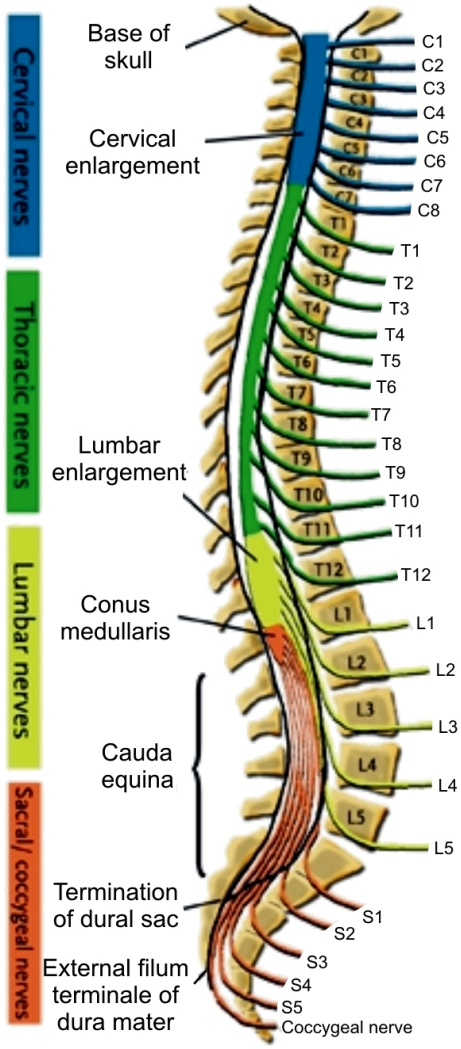

Figure 2.6.: Entry levels of spinal nerves into the spinal canal and into the spinal cord respectively.
The enlargements at the cervical/thoracic levels correspond with entry and exit of fibers supplying the upper/lower limbs.

At the intervertebral foramina (bony canals formed by two adjacent vertebrae) the dorsal and the ventral roots join to form the spinal nerves. The resulting 31 pairs of spinal nerves divide the cord into 8 cervical (C), 12 thoracic (T), 5 lumbar (L), 5

sacral (S) and 1 coccygeal segments, named and numbered according to the vertebra at which they exit the spinal column. In the cervical region of the spinal cord, the spinal nerves exit above the vertebrae with equal number, except for the C8 spinal nerve which exits below the C7 vertebra. From T1 downwards, all spinal nerves exit below their equivalent numbered vertebrae (Figure 2.6). Four nerve roots emerge from each spinal cord segment, a dorsal and a ventral root on each side. They are contained within the spinal canal, bathed in cerebrospinal fluid and follow a lateral or, in the lower levels of the spinal cord, a descending course to the intervertebral foramen.

At its lower (caudal) end, the spinal cord tapers to form the conus medullaris and terminates at the level of the first or second lumbar vertebra. About 90 per cent of spinal cords have shown to end at the disc-space between those two vertebral bodies [Lang 1984]. This results in long spinal roots for lumbar and sacral nerves. These roots are called the cauda equina because their shape resembles a horse tail.

The spinal cord is covered and protected by three membraneous coverings (meninges) as well as cerebrospinal fluid and epidural fat. The cerebrospinal fluid is electrically well conducting and is located between the cord and the thick outer membrane called dura mater spinalis, which in turn is surrounded by fat within the spinal canal.

2.4. Relation Between Excited Spinal Root Fibers and Corresponding Muscle Responses

One of the factor that affects the excitability of neurons is their distance to the stimulating electrode. For a given electrode position the spinal root fibers are excited in a definite order. The theoretical results from the computations in this study should help to interpret the recruitment order of the corresponding muscle responses. Thus, a relation is required between the sequence of excited neural structures and the resulting order of muscle responses.
Group Ia afferent fibers innervating muscle spindles in the lower limb muscles reach a certain lumbar spinal cord segment via the corresponding posterior root (=dorsal root). In the gray matter of the spinal cord these fibers make monosynaptic excitatory connections with motor neurons of the ventral roots supplying the same muscle (that contains the muscle spindle) and with those supplying synergists (Figure 2.7) [Brown 1981].

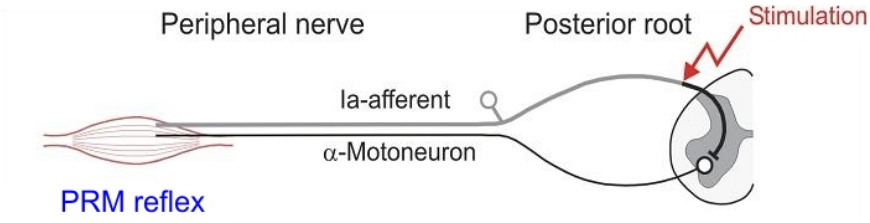

Figure 2.7.: Illustration of a posterior root - muscle reflex arc.

The motor neurons of each spinal cord segment supply certain muscles. Consequently the excitation order of dorsal roots is related to the sequence of responses of corresponding muscle groups (Figure 2.8). The segmental arrangement of innervation of lower limb muscles is adopted from Minassian [Minassian 2000, Rattay et al. 2000]: Quadriceps and adductor are innervated by the segments L2, L3, L4, hamstring by L3, L4, L5, S1, tibialis anterior by L4 and L5, and triceps surae by the segments L5, S1 and S2.

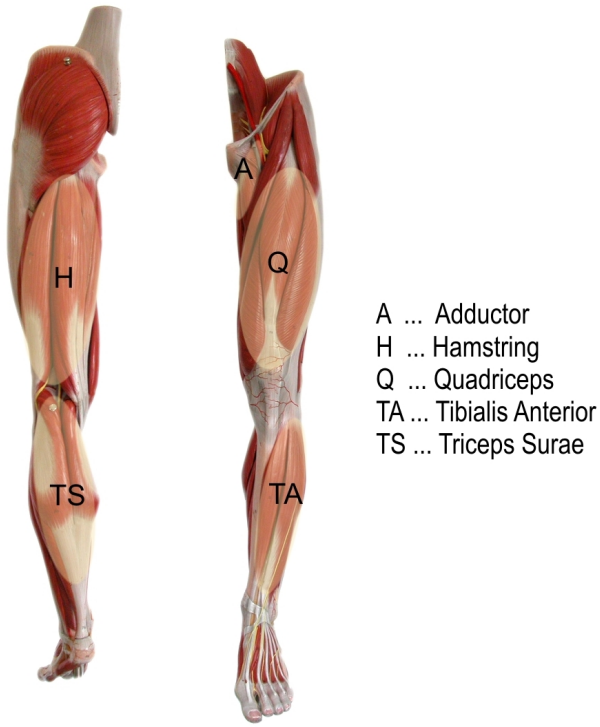

Figure 2.8.: Main lower limb muscles.

The above mentioned relation does not hold when dorsal column fibers are excited. Instead, electrical stimulation of these fibers elicits a tingling sensation (paraesthesia) in the corresponding area of skin which they supply [Holsheimer 1998].

2.5. Geometry of Spinal Root Fibers and Dorsal Column Fibers

The input data for the nerve fiber models are arrays of voltage values obtained by evaluating the potential distribution, calculated by the finite element method, along the trajectories of representative nerve fibers. Therefore the geometry of the simulated target neurons has an essential influence on the results. However, exact information about the three-dimensional geometry of fibers simulated in this study cannot be found in literature. Neither can the positions of the spinal cord segments, where the corresponding spinal root fibers originate, be accurately identified.

Anatomical photographs and the findings from [Wall et al. 1990, Cohen et al. 1991, Hasegawa et al. 1996, Brown 1981, Smith and Deacon 1984, Lang 1984] are used to define the standard trajectories of the simulated fibers (Figure 2.9).

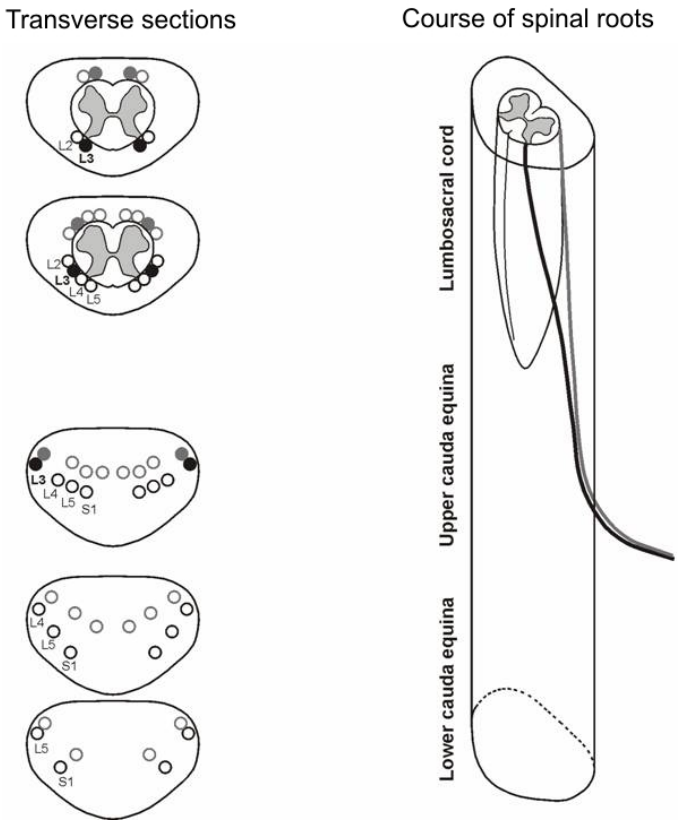

Figure 2.9.: Root fiber trajectories derived from cross sections. Standard dorsal and ventral root fiber trajectories (right) are obtained from root fiber identification in anatomical cross sections at several levels (left).

The positions of spinal cord segments with respect to the vertebrae as well as their lengths are assumed according to Minassian, who derived two opposing models of segment arrangement using the results of several authors [Minassian 2000, Rattay et al. 2000]. Figure 2.10 (A) shows the segment arrangement model constructed from spinal root fiber identification in four cross sections [Wall et al. 1990] under the assumption that segments with fibers passing the observed cross-section are located completely above this cross section level. In Figure 2.10 (B) the spinal cord geometry according to data from [Lang and Geisel 1983] is presented. The grey and white bars represent mean segment levels and their variations.

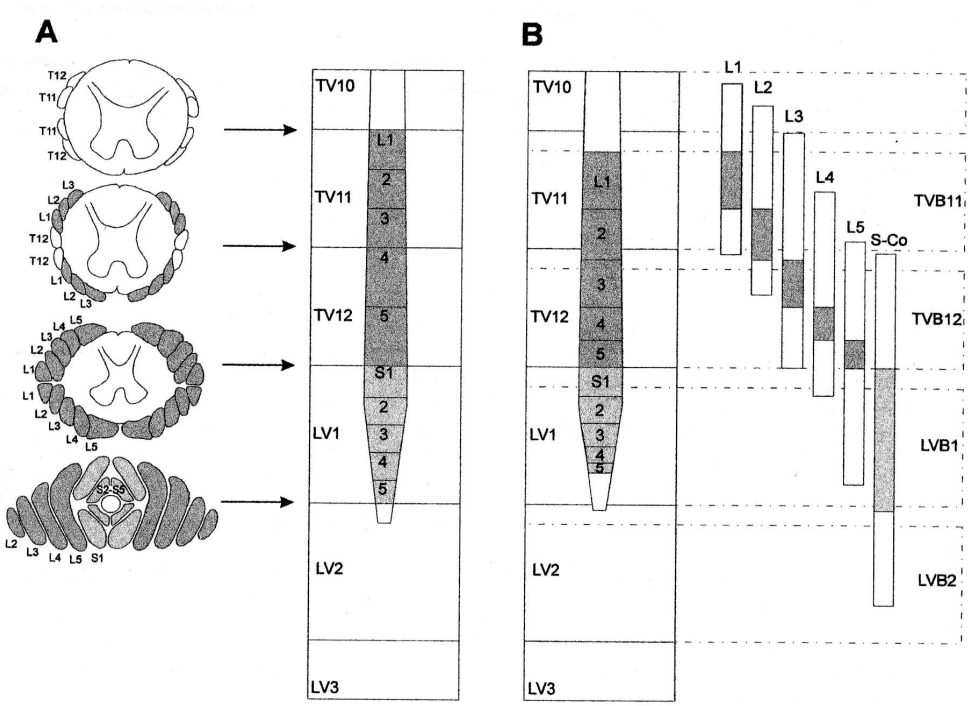

Figure 2.10.: Relationship between spinal cord and vertebral segment levels. TVB: thoracic vertebral bone, LVB: lumbar vertebral bone.

Dorsal root (DR) fibers and dorsal column (DC) fibers are part of the same primary afferent fiber system. Upon entering the spinal cord the majority of DR fibers run into the lateral parts of the dorsal columns and bifurcate into an ascending and a descending DC branch. The DC fibers gradually shift medially and issue collateral branches perpendicular to the main axon into the dorsal gray matter where they freely arborize (Figure 2.11) [Brown 1981, Fyffe 1984, Smith and Deacon 1984].

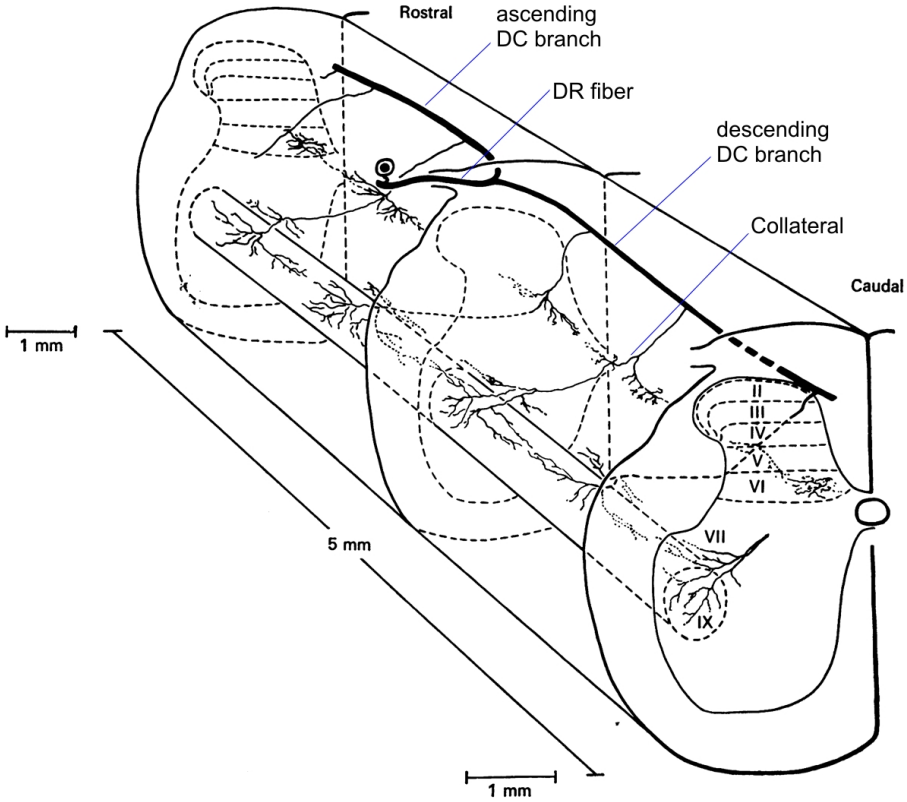

Figure 2.11.: Schematic representation of the arrangement of Ia afferent fiber collaterals in the lumbosacral cord of the cat. The figure is drawn to scale and shows the main features of the collateral morphology [Brown 1981]. The laminae of the gray matter are marked and numbered.

Another major factor influencing the excitability of a nerve fiber is its diameter. Fibers with larger diameters are easier to activate. Therefore, values in the upper range of the diameter distribution are used. Spinal root fibers are given diameters of up to 20μm, DC fibers 80% of that value. Assuming a linear relationship between fiber diameter and conduction velocity this is in accordance with Desmedt and Cheron who found a drop in propagation velocity of about 19% after bifurcation of the DR fiber [Brown 1981, Desmedt and Cheron 1980, Hongo et al. 1987, Hursh 1939]. Collaterals are assigned diameters of one third of the DC fiber diameter value [Hongo et al. 1987].

3. Volume Conductor Model

During the stimulation pulse, a potential difference between the electrode contacts causes ionic current to flow from the anode to the cathode through the intermediate anatomical structures - the volume conductor. The resulting electric potential distribution is determined by the geometry of these structures and their electrical properties. Equations that describe electrical current flow and the potential distribution in biological tissues are introduced. Subsequently, the mathematical technique used to solve these equations - the FE Method - and the implementation of the model using the software product COMSOL Multiphysics (former FEMLAB) are presented.

3.1. Problem Formulation

The current flowing through the electrodes and the intermediate tissues can be mathematically described with Maxwell's equations. For electrostatic problems in dielectric volume conductors, an electric field, $\mathbf{E}$, can be described in terms of the gradient of a scalar potential field, $\mathbf{\Phi}$ [Klepfer et al. 1997].

$$\mathbf{E} = -\nabla \mathbf{\Phi} \tag{3.1}$$

Applying Gauss' law (3.2) to the continuity equation (3.3) yields (3.4), where $\mathbf{D}$ is the electric displacement field, ρ the charge density, and $\mathbf{J}$ the electric current density.

$$\nabla \cdot \mathbf{D} = \rho \tag{3.2}$$

$$\nabla \cdot \mathbf{J} + \frac{\partial \rho}{\partial t} = 0 \tag{3.3}$$

$$\nabla \cdot \left[\mathbf{J} + \frac{\partial \mathbf{D}}{\partial t} \right] = 0 \tag{3.4}$$

It has been shown that currents within the body are essentially conduction currents [Schwan and Kay 1957]. Therefore, the displacement current density $\frac{\partial \mathbf{D}}{\partial t}$ is neglected, which results in a quasistatic approximation of equation (3.4). The volume conductor is considered purely resistive.

Thus, the current density associated with the electric field is given by Ohm's law

$$\mathbf{J} = \sigma \mathbf{E}, \tag{3.5}$$

where the electrical conductivity σ is represented mathematically as a 3 x 3 symmetric tensor.

Substituting (3.5) into the quasistatic approximation of equation (3.4), and (3.1) into (3.5), we obtain

$$\nabla \cdot (\sigma \nabla \mathbf{\Phi}) = 0 \qquad \text{in } \Omega, \tag{3.6}$$

with Ω being the bounded solution domain. The equation (3.6) is a general form of Laplace's equation.

Including Dirichlet and Neumann boundary conditions a boundary value problem is formulated.

- Dirichlet boundary condition:

$$\mathbf{\Phi} = \Phi_0 \qquad \text{on } \Gamma_D \subseteq \Gamma, \tag{3.7}$$

  which means $\mathbf{\Phi}$ is constant and equal to the externally applied potentials Φ_0 on Γ_D. (Γ is the boundary of Ω.) This condition is used at the electrode surfaces.

- Neumann boundary condition:

$$(\sigma \nabla \mathbf{\Phi}) \cdot \mathbf{n} = 0 \qquad \text{on } \Gamma_N \subseteq \Gamma, \tag{3.8}$$

  which states that the current density perpendicular to the surfaces Γ_N is zero. This condition is used at the body surface, no current flows out of the body. ($\Gamma_D \cup \Gamma_N = \Gamma$)

3.2. Numerical Methods

This volume conductor problem which includes inhomogeneities, anisotropy and a complex geometry can only be solved numerically. The finite element method (FEM) is applied to calculate the steady-state solutions. It is the preferred method for problems with irregular, inhomogeneous domains and mixed boundary conditions, suitable for representing nonlinearity and true anisotropy [Johnson 1997]. The trade-off are the relatively high computational costs for detailed models.

In the finite element method, the solution domain is discretized (meshed) into a number of uniform or nonuniform finite elements, usually tetrahedrons, that are connected via nodes. An estimate of the potential field over each element is computed, taking into account the material properties of each individual element. Applying the FEM to the problem (3.6) with boundary conditions (3.7), (3.8) results in a system of linear equations, $A\Phi = b$, which is subsequently solved for the unknown variable Φ. The solution of this system provides the potential at each node in the discretized model geometry.

The formulation of the finite element approximation starts with the Galerkin approximation [Johnson 1997]: Equation (3.6) can be rewritten as

$$L\mathbf{\Phi} = 0, \tag{3.9}$$

where L is the (linear) differential operator, $L = \nabla \cdot (\sigma \nabla)$. An equivalent statement of the previous equation is:

$$\text{Find } \mathbf{\Phi} \text{ such that} \quad (L\mathbf{\Phi}, \mathbf{\Psi}) = 0. \tag{3.10}$$

Here $\mathbf{\Psi}$ is an arbitrary *test function*, which can be thought of physically as a virtual potential field, and $(\phi, \psi) := \int_\Omega \phi\psi d\Omega$ denotes the inner product in $L_2(\Omega)$.

Applying Green's theorem and the product rule, equation (3.10) can be written as

$$\left\langle \frac{\partial \mathbf{\Phi}}{\partial \mathbf{n}}, \mathbf{\Psi} \right\rangle - (\sigma \nabla \mathbf{\Phi}, \nabla \mathbf{\Psi}) = 0, \tag{3.11}$$

where $\langle \phi, \psi \rangle := \int_\Gamma \phi\psi d\Gamma$ denotes the inner product on the boundary Γ. With Dirichlet (3.7) or Neumann (3.8) boundary conditions specified on Γ, and test functions which vanish at the boundaries where $\mathbf{\Phi} = \Phi_0$ (Dirichlet), the *weak form* of equation (3.6) is obtained

$$(\sigma \nabla \mathbf{\Phi}, \nabla \mathbf{\Psi}) = 0 \tag{3.12}$$

Let V_h be a finite dimensional subspace of $L_2(\Omega)$ with basis functions Ψ_i, $i = 1, \ldots, N$. The *Galerkin approximation* of the solution $\mathbf{\Phi}$ in equation (3.12) is defined as the element $\mathbf{\Phi}_h \in V_h$ which satisfies

$$(\sigma \nabla \mathbf{\Phi}_h, \nabla \Psi_j) = 0 \qquad \forall \Psi_j \in V_h \tag{3.13}$$

$\mathbf{\Phi}_h$ can be expressed in a unique way as a linear combination of the basis functions $\Psi_i \in V_h$

$$\mathbf{\Phi}_h(\mathbf{x}) = \sum_{i=1}^{N} \Phi_i \Psi_i(\mathbf{x}) \qquad (\mathbf{x} \in \Omega) \tag{3.14}$$

Inserting (3.14) in equation (3.13) the problem of finding the Galerkin approximation reduces to solving a system of N equations:

$$(\sigma \nabla \sum_{i=1}^{N} \Phi_i \Psi_i, \nabla \Psi_j) = \sum_{i=1}^{N} \Phi_i (\sigma_{ij} \nabla \Psi_i, \nabla \Psi_j) = 0 \qquad j = 1, \ldots, N \tag{3.15}$$

In matrix form, the preceding system can be written as $A\Phi = b$, where $A = (a_{ij})$ is called the *global stiffness matrix* with elements $a_{ij} = (\sigma_{ij} \nabla \Psi_i, \nabla \Psi_j)$, while $b_j = 0$, $j = 1, \ldots, N$. For volume conductor problems, A contains all the geometry and conductivity information of the model. The matrix A is symmetric and positive definite, thus it is nonsingular and the equation system has a unique solution.

Since L is positive definite and self adjoint [i.e. $(L\mathbf{\Phi}, \mathbf{\Phi}) \geq \alpha(\mathbf{\Phi}, \mathbf{\Phi}) > 0$ for some positive constant α and $(L\mathbf{\Phi}, \mathbf{\Psi}) = (\mathbf{\Phi}, L\mathbf{\Psi})$, respectively] we can define a space E with an inner product defined as $(\mathbf{\Phi}, \mathbf{\Psi})_E := (L\mathbf{\Phi}, \mathbf{\Psi})$ and norm (the so-called energy norm)

$$\|\mathbf{\Phi}\|_E := (\mathbf{\Phi}, \mathbf{\Phi})_E^{\frac{1}{2}} = \left[\int_\Omega (\nabla \mathbf{\Phi})^2 d\Omega \right]^{\frac{1}{2}} \tag{3.16}$$

The solution of equation (3.10) satisfies

$$(L\mathbf{\Phi}, \Psi_j) = 0 \qquad \forall \Psi_j \in V_h \tag{3.17}$$

and the approximate Galerkin solution $\mathbf{\Phi}_h$ obtained by solving equation (3.13) satisfies

$$(L\mathbf{\Phi}_h, \Psi_j) = 0 \qquad \forall \Psi_j \in V_h \tag{3.18}$$

Subtracting equation (3.17) from equation (3.18) yields

$$(L(\mathbf{\Phi}_h - \mathbf{\Phi}), \Psi_j) = 0 = (\mathbf{\Phi}_h - \mathbf{\Phi}, \Psi_j)_E \qquad \forall \Psi_j \in V_h \tag{3.19}$$

The difference $\mathbf{\Phi}_h - \mathbf{\Phi}$ denotes the error between the solution in the infinite dimensional space $L_2(\Omega)$ and the finite dimensional space V_h. Equation (3.19) states that the error is orthogonal to all basis functions spanning the space of possible Galerkin solutions. Consequently it must be the minimum error. The Galerkin approximation is an orthogonal projection of the true solution $\mathbf{\Phi}$ onto the given finite dimensional space of possible approximate solutions. Therefore it is the best approximation in the energy space E. Since the operator is positive definite, the approximate solution is unique.

Now, using the weak formulation of the problem and the Galerkin procedure the FEM can be applied. The solution domain is discretized using tetrahedral elements that are connected via nodes. Defining basis functions Ψ_i, $i = 1, \ldots, N$ as linear piecewise continuous functions, each of which takes the value 1 at one node point $\mathbf{x}_i$ and zero at all the other node points, the finite dimensional subspace $V_h \subset V = \{\mathbf{\Psi} : \mathbf{\Psi}$ is continuous on $\Omega, \nabla\mathbf{\Psi}$ is piecewise continuous on $\Omega\}$ is created.

These basis functions Ψ_i are used in the equation system (3.15), or $A\Phi = b$, which is solved for $\Phi = (\Phi_1, \ldots, \Phi_N)$. The N unknowns Φ_i, $i = 1, \ldots, N$ are the coefficients in the linear combination (3.14) of the finite element approximation $\mathbf{\Phi}_h$ and satisfy

$$\Phi_i = \mathbf{\Phi}_h(\mathbf{x}_i) \tag{3.20}$$

Therefore, the Φ_i represent the electrostatic potentials at the nodes $\mathbf{x}_i$.
Furthermore, the basis functions defined above differ from zero for only a few intervals each, which results in a *sparse* global stiffness matrix A (i.e. only a few of its entries are nonzero).

3.3. Implementation of the Model

In this study the finite element software package COMSOL Multiphysics is used to solve the volume conductor problem (3.6) subject to boundary conditions (3.7) and (3.8) numerically. This can be accomplished selecting the Multiphysics module *Conductive Media DC*. Once the geometry of the 3D model is defined, the solution domain of the volume conductor is discretized into a number of finite tetrahedral volume elements, which is automatically done by a mesh generator. The number of nodes and mesh elements used in the discretization determines the accuracy of the solution as well as the time and memory demand for the computations. To maximize the node density, only one half of the model geometry is used due to its symmetry about the sagittal plane. Within the model geometry, conductivity values have to be specified for all subdomains representing anatomical tissues relevant for the simulation. Appropriate boundary conditions, Neumann and Dirichlet respectively, are assigned to the surfaces. Finally, the solution is calculated by a designated solver.

3.3.1. Model Geometry

The geometry of the spinal cord and its surrounding anatomical structures are a major factor determining the 3D distribution of the electric potential caused by the electrodes. The relevant structures which make up the model include: electrode compartments, skin, a fat layer, a general thorax compartment, paraspinal muscles, the lumbar spine, vertebral discs, epidural fat, cerebrospinal fluid, white matter and gray matter. Most of the geometry is taken from a model [Szava 2006], which is based on information from cross-section photographs at the intervertebral level T12 - L1, and from FE studies on the mechanically loaded vertebral column. Skin and electrodes are modeled as separate 2mm thick compartments (Figures 3.1, 3.2). This is done to obtain a realistic overall impedance, see Section 3.3.2. The electrode positions correspond to the electrode setup used in electrophysiological studies [Minassian et al. 2007a, Hofstoetter et al. 2008], with the round stimulating electrodes placed over the T11 - T12 vertebral processes (see Figure 1.1). From top to bottom, the model measures 39cm. There is a 12cm distance from the top to the upper edge of the round stimulating electrode at the back and from the bottom to the lower edge of the reference electrode at the front, respectively. The effects of refining the thorax geometry by including further anatomical structures are investigated in 5.3.

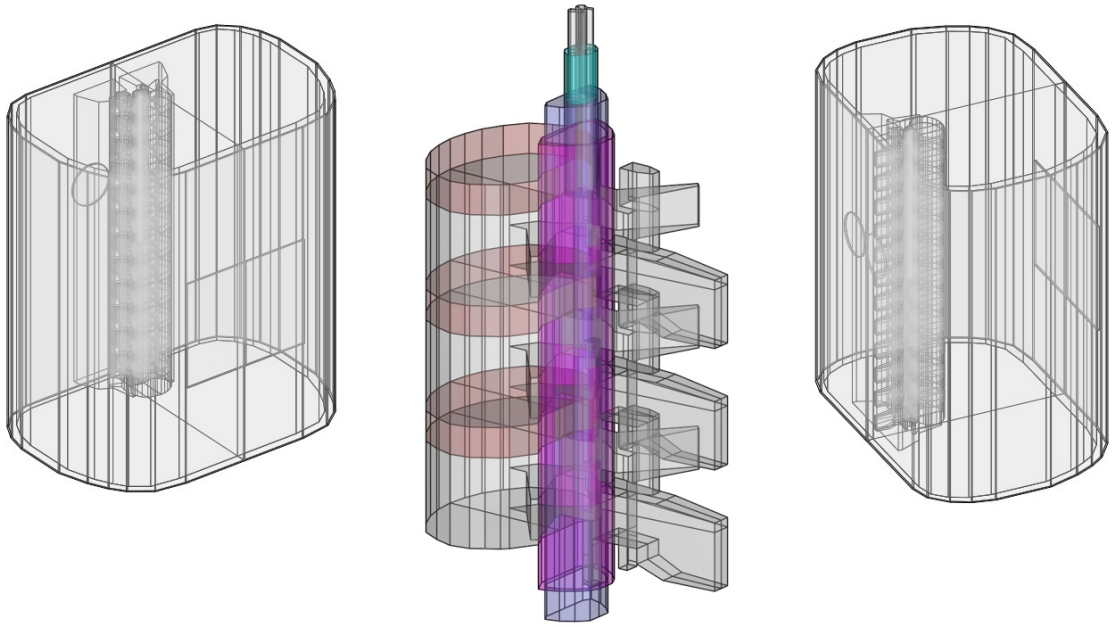

Figure 3.1.: The geometry of the 3D model (left and right) and the geometry of the vertebral column including the epidural fat compartment, cerebrospinal fluid, white matter and grey matter, 3D view (middle)

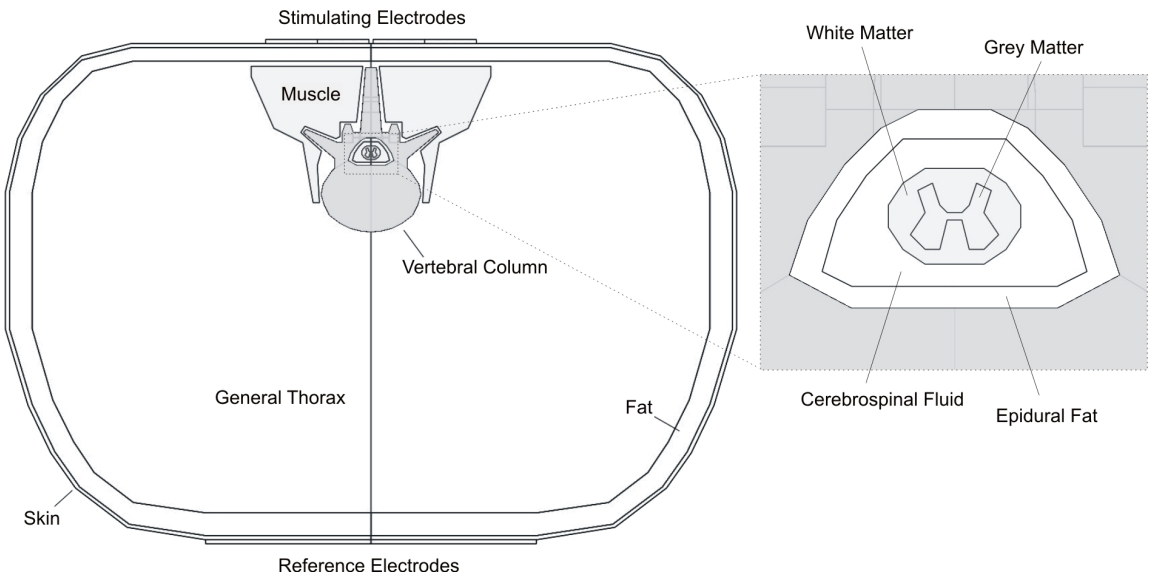

Figure 3.2.: The model geometry in transverse section with zoomed view of spinal canal.

3.3.2. Tissue Conductivities

The electrical conductivities of the various compartments of the model, which represent different anatomical structures made up of biological tissues, constitute another large influence to the electric potential distribution. Due to the capacitance of cell membranes the conductivity of biological tissues varies with the frequency content of the electrical signal. Accordingly, tissue conductivities increase when the duration of a stimulating pulse is reduced [Holsheimer 1998]. For rectangular pulses of 1 – 2 ms duration, common in tSCS, the principal frequency components are 0.25 – 0.5 kHz. The range of σ values corresponding to those frequencies are given in Table 3.1, as well as the 'standard' values, used in the simulations for this study.

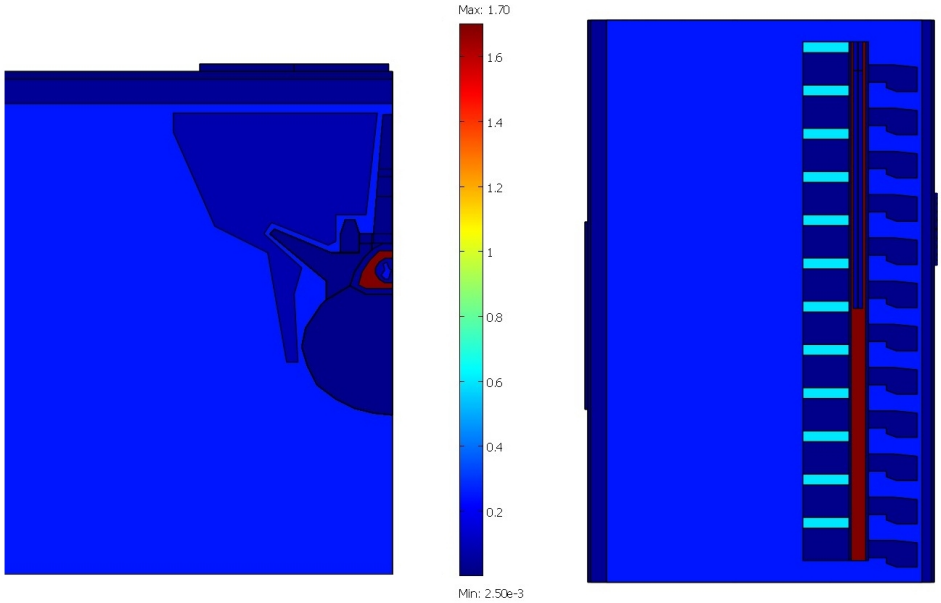

Figure 3.3.: Conductivities (color coded) of the various anatomical structures in the model according to Table 3.1.

All compartments are purely resistive and except for white matter and muscle the conductivities are isotropic. These two tissues consist of well defined long fibers, which results in notable differences between transversal and longitudinal conductivities. The 'standard' values for gray matter, white matter, csf, fat, bone, vertebral discs, and the general thorax are taken from various spinal cord stimulation modeling studies [Coburn and Sin 1985, Holsheimer 1998, Struijk et al. 1991, 1992, 1993a, Rattay et al. 2000, Szava 2006]. The anisotropic muscle conductivities are acquired from [Malmivuo and Plonsey 1995, Foster and Schwan 1989, Miklavcic et al. 2006].

The 2mm thick electrode compartments which include the electrode-skin interface are given values corresponding to a resistance of 100Ω for the stimulating electrode applied at the lower back. Based on impedance measurements performed on two subjects using the electrode setup simulated in this study, the 'standard' skin conductivity is chosen to obtain an overall impedance in the range of 700 - 900 Ω, while being within the limits of measured σ_{skin} values [Gabriel et al. 1996, Raicu et al. 2000]. The various anatomical structures with assigned conductivities are illustrated in Figure 3.3.

Material	**Conductivity [S/m]**			**References**
	Min	Standard	Max	
Electrode interface	0.0001	0.01	1	Overall impedance measurements
Skin	0.0001	0.0025	0.003	
Fat	0.002	0.04	0.1	[Malmivuo and Plonsey 1995, Geddes and Baker 1967]
General thorax	0.2	0.25	0.3	[Coburn and Sin 1985, Geddes and Baker 1967, Rattay et al. 2000, Szava 2006]
Muscle (transversal)	0.04	0.08	0.17	[Malmivuo and Plonsey 1995, Foster and Schwan 1989]
Muscle (longitudinal)	0.2	0.5	0.8	[Malmivuo and Plonsey 1995, Foster and Schwan 1989]
Vertrebral bone	0.01	0.02	0.03	[Szava 2006]
Vertebral disc	0.47	0.6	0.65	[Gu et al. 2002, Szava 2006]
Epidural fat	0.002	0.04	0.1	[Struijk et al. 1991, 1992, 1993a]
Cerebrospinal fluid	1.5	1.7	1.7	[Rattay et al. 2000, Holsheimer 1998]
White matter (transversal)	0.083	0.083	0.083	[Rattay et al. 2000, Holsheimer 1998]
White matter (longitudinal)	0.6	0.6	0.72	[Struijk et al. 1991, 1992, 1993a]
Grey matter	0.17	0.23	0.23	[Struijk et al. 1991, 1992, 1993a]

Table 3.1.: Conductivities of different tissues. The columns 'Min' and 'Max' are extreme values from [Foster and Schwan 1989, Gabriel et al. 1996, Geddes and Baker 1967, Gu et al. 2002, Kuhn 2008, Miklavcic et al. 2006, Raicu et al. 2000]. The 'Reference' column refers to the 'standard' values.

3.3.3. Boundary Conditions

Neumann boundary conditions (3.8) are assigned to the external surface of the skin layer, to the sagittal symmetry plane, and to the top and bottom surfaces. The effects when using an extended model, with two prismatic volumes added on the top and bottom of the main volume, are investigated in 5.3.
Dirichlet boundary conditions (3.7) are assigned to the outer electrode surfaces. -50V are applied to the stimulating round electrode, 0V to the rectangular reference electrode. To obtain the potential distribution along the nerve fiber pathways for any voltage strength or the other polarity, the results calculated by the finite element method are multiplied by the corresponding factor.

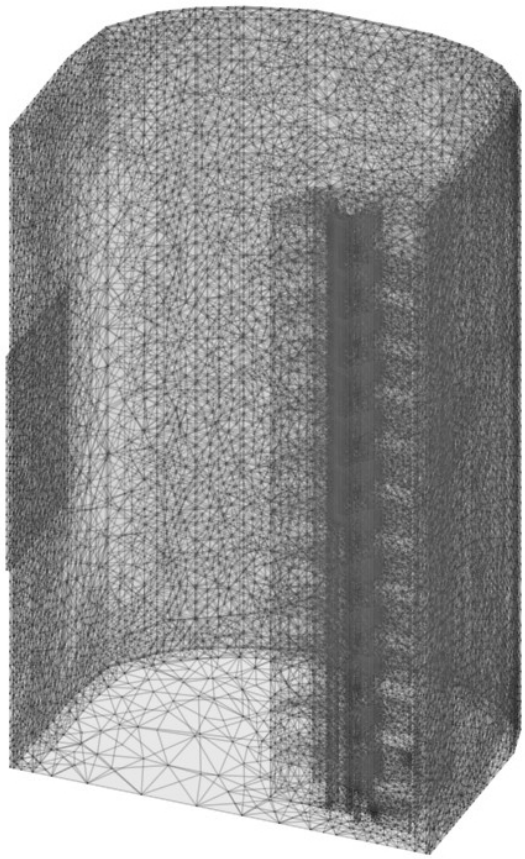

Figure 3.4.: Meshed model with 440476 elements and 86432 nodes.

3.3.4. Solution of the VC Problem

The 3D model was discretized into 440476 mesh elements connected by 86432 nodes, at which the solution was computed (Figure 3.4). For the calculations the *Conjugate gradients* iterative linear system solver and the *SSOR* (Symmetric Successive Over-Relaxation) preconditioner were selected due to their memory efficiency.

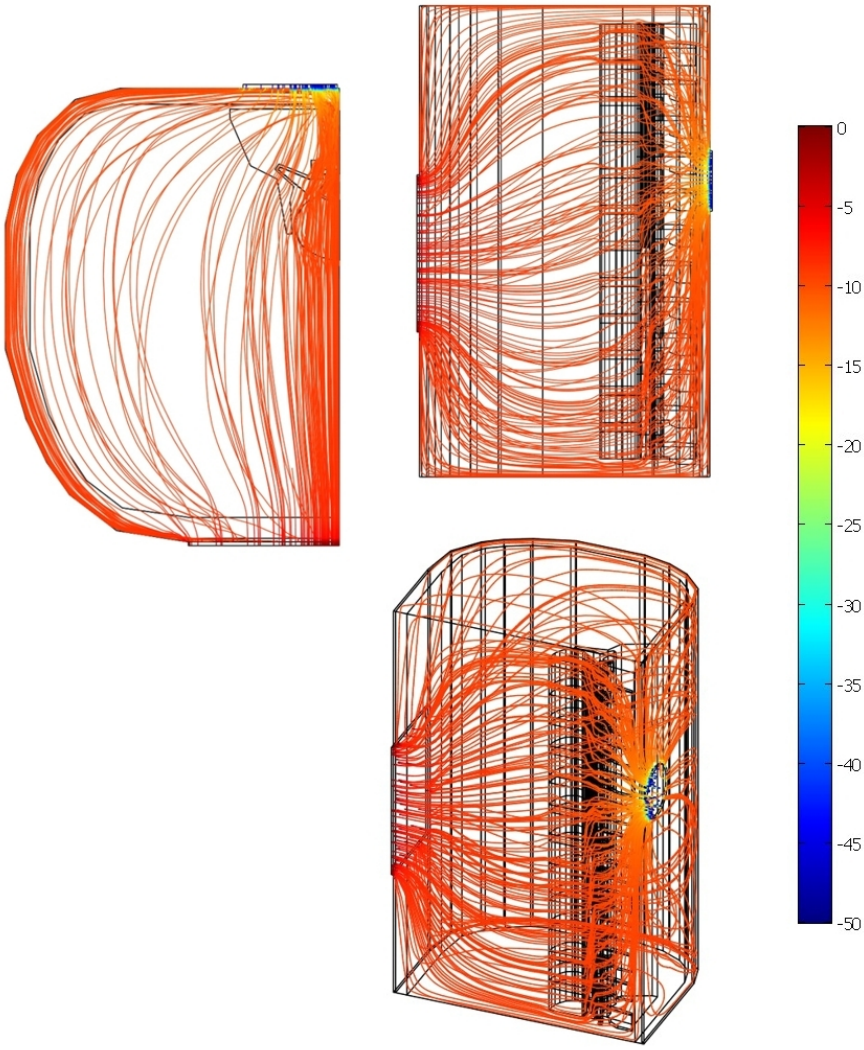

Figure 3.5.: Calculated total current density, color code illustrates the electrical potential. Top left: view from above (transversal cut), top right: lateral view (sagittal cut), bottom: 3D view. The computations were performed using an Intel Core Duo T2300 1.66 GHz processor and 1GB DDR2 SD memory. It took 296 iterations in 270 seconds to solve the problem. The overall impedance in the model is 746 Ω, the average conductivity is 0.211S/m.

4. Nerve Fiber Model

To investigate the main influences on the excitation process in tSCS and the order in which target neurons are excited using different electrode arrangements a nerve fiber model was established that represents the neuron's response behavior to external stimuli along its axon. The electrical potentials, calculated by the finite element method in a first step (see Chapter 3) are evaluated along the pathways of different target neurons. These voltage profiles then serve as the input data V_e (extracellular potentials) for the nerve fiber model. The activating function, a useful and uncomplicated approach to predict AP generation, is introduced in 4.1. In Section 4.2, equations describing the complex behavior of the ion channels in the active parts of the nerve fiber are presented. At the end of this chapter, the parameter values used in the model are given.

Analysis of different substructures of a neuron has shown that the most excitable part is the myelinated axon. The soma region is expected to get only little excited comparatively, which is a consequence of the high value of the membrane capacitance of the soma compared to that of the small nodal area [Rattay 1998]. Therefore, the model is restricted to the myelinated axon.

In order to simulate neural reactions the nerve fiber is divided into compartments of certain lengths and each compartment is represented by an electrical circuit. Node of Ranvier segments alternate with internodes comprising the myelin sheath.
Since the model is made up of an electrical network in which the current efflux of one compartment is the current influx for the next, Kirchhoff's first law can be applied. The current to the central point of the n-th compartment consists of the following components: capacitive current $I_{C,n}$, ion currents $I_{ion,n}$ across the membrane and ohmic currents $I_{axon,n}$ from the neighbors.
The transmembrane current at compartment n is equal to the sum of the capacitive and ionic currents and, according to Kirchhoff, equal to the intra-axonal currents [McNeal 1976, Rattay 1999].

Therefore,

$$\underbrace{C_{m,n}\frac{d(V_{i,n}-V_{e,n})}{dt}}_{I_{C,n}} + I_{ion,n} + \underbrace{\frac{V_{i,n}-V_{i,n-1}}{R_{a,n}/2+R_{a,n-1}/2} + \frac{V_{i,n}-V_{i,n+1}}{R_{a,n}/2+R_{a,n+1}/2}}_{I_{axon,n}} = 0 \tag{4.1}$$

Introducing the reduced membrane voltage $V = V_i - V_e - V_{rest}$ leads to the following system of differential equations for calculating the time-course of V_n in each compartment:

$$\begin{aligned}\frac{d\,V_n}{dt} = \frac{1}{C_{m,n}}\Bigg[-I_{ion,n} &+ \frac{V_{n-1}-V_n}{R_{a,n-1}/2+R_{a,n}/2} + \frac{V_{n+1}-V_n}{R_{a,n+1}/2+R_{a,n}/2} + \dots \\ &+ \frac{V_{e,n-1}-V_{e,n}}{R_{a,n-1}/2+R_{a,n}/2} + \frac{V_{e,n+1}-V_{e,n}}{R_{a,n+1}/2+R_{a,n}/2} + \dots\Bigg]\end{aligned} \tag{4.2}$$

$C_{m,n}$ denotes the membrane capacitance and $R_{a,n}$ the axonal resistance of the n-th compartment. Their values depend on the axon segment diameter d_n and length l_n as follows:

$$C_{m,n} = c_m\, d_n \pi\, l_n \tag{4.3}$$

$$R_{a,n} = \rho_a\, \frac{4\, l_n}{d_n^2 \pi}, \tag{4.4}$$

where c_m is the specific membrane capacity and ρ_a the axoplasmatic resistivity.

The dots in equation (4.2) stand for terms similar to the previous ones that have to be added in cases of more than two neighbor elements, e.g. in branching regions. For the first and last compartments, equation (4.2) has a reduced form.

For nodal compartments additional differential equations have to be solved in order to calculate the ionic membrane current $I_{ion,n}$. The CRRSS (Chiu-Ritchie-Rogart-Stagg-Sweeney) model was used to simulate the ion channel dynamics in these active parts of the axon [Chiu et al. 1979, Sweeney et al. 1987], see Section 4.2.

Internodal compartments are elements with passive membranes and are assumed to have a constant membrane conductance $G_{m,n}$. In these cases $I_{ion,n}$ can be written as (4.5). Knowing the specific capacity c_m and the conductivity g_m of the membrane we can approximate the variables $C_{m,n}$ and $G_{m,n}$, which depend on the number N of layers of myelin wrapped around the cylinders with diameter d_n and length l_n [Rattay 1995].

$$I_{ion,n} = G_{m,n}\, V_n \tag{4.5}$$

$$C_{m,n} = \frac{c_m}{N}\, d_n \pi\, l_n \tag{4.6}$$

$$G_{m,n} = \frac{g_m}{N}\, d_n \pi\, l_n \tag{4.7}$$

Since N influences the velocity by which an AP is propagated, it was given the proper value to achieve the adequate propagation velocity dependent on the fiber diameter [Hursh 1939], see Table 4.1.

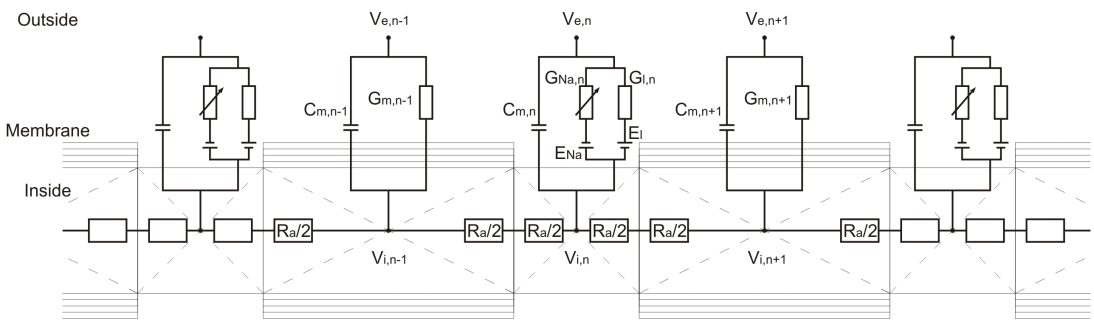

Figure 4.1.: Electrical network model of a myelinated nerve fiber. An internode is represented by a single compartment with a constant membrane conductance G_m. The active parts of the axon, the nodes of Ranvier, are modeled using equations which describe the complex gating mechanism of sodium ion channels in the membrane. G_{Na} is shown with an arrow indicating that it depends on the voltage. The batteries E_{Na} and E_l result from differences in ion concentrations between the intracellular and extracellular fluid.

The voltages at the inside $V_{i,n}$ and at the outside $V_{e,n}$ of the n-th compartment are represented by a mean value (Figure 4.1). This means that, from the numerical point of view, the length of a cylindrical compartment with diameter d is restricted by its *space constant* λ,

$$\lambda = \sqrt{\frac{d}{4\,\rho_a g_m}}. \tag{4.8}$$

If the compartment length is below $\lambda/4$, the error compared to the solution of the continuous cable equation is of the order of 1% [Rattay 1999].

Internodal lengths are taken 100 times the fiber diameter D, as opposed to node lengths of only $1.5\,\mu m$. Inserting the parameter values from Table 4.1 in (4.9) reveals that even for the largest simulated fibers, with $D = 20\mu m$, the internode can be represented by a single compartment:

$$\begin{aligned} 100\,D &< \frac{\lambda}{4} \\ D &< 0.0155\,cm \end{aligned} \tag{4.9}$$

4.1. Activating Function

Considering equation (4.2) it can be noticed that the direct stimulating influence of the extracellular potential on compartment n is

$$f_n := \frac{1}{C_{m,n}} \left[\frac{V_{e,n-1} - V_{e,n}}{R_{a,n-1}/2 + R_{a,n}/2} + \frac{V_{e,n+1} - V_{e,n}}{R_{a,n+1}/2 + R_{a,n}/2} + \dots \right], \tag{4.10}$$

which is the formulation of the *activating function* for neurons of arbitrary shape [Rattay 1999]. The physical dimension of f_n is V/s or mV/ms. It represents the velocity of membrane voltage change in each compartment that is activated by the extracellular field, i.e. f_n is the slope of the membrane voltage V_n at the beginning of the stimulus.

In case of a long homogeneous fiber (i.e. an unmyelinated axon or a muscle fiber) with cylindrical compartments of constant diameter d and length l, the activating function becomes proportional to the second spatial derivative of V_e along the axon. Substituting $C_{m,n} = c_m\, d\pi\, l$ and $R_{a,n} = \rho_a\, \frac{4\,l}{d^2\pi}$ in equation (4.10) leads to

$$f_n = \frac{d}{4\,\rho_a c_m} \frac{V_{e,n-1} - 2\,V_{e,n} + V_{e,n+1}}{l^2} \tag{4.11}$$

and with $l \to 0$ and x as fiber length coordinate, the activating function can be written as

$$f(x) = \frac{d}{4\,\rho_a c_m} \frac{\partial^2 V_e}{\partial\, x^2}. \tag{4.12}$$

The simple calculation of the activating function does not require knowledge of the behavior of the ion channels in the neural membranes and can be used to predict AP generation. An axon becomes depolarized in regions with $f > 0$ and hyperpolarized in regions with $f < 0$. The origin of an artificially generated AP is expected in the region where f has its maximum value.

4.2. Membrane Equations

The CRRSS model, which describes the nonlinear gating mechanisms of ion channels across the unmyelinated neuronal membrane, was used to calculate $I_{ion,n}$ at the nodes. The model incorporates sodium and leakage currents, but disregards potassium channels as they were found to be less important in the excitation process of myelinated mammalian nerves [Sweeney et al. 1987], and it is directly applicable for a temperature of 37°C:

$$I_{ion,n} = \underbrace{G_{Na,n}\, m^2 h\, (V_n - E_{Na})}_{I_{Na}} + \underbrace{G_{l,n}\, (V_n - E_l)}_{I_l} \tag{4.13}$$

$$G_{Na,n} = g_{Na}\, d_n \pi\, l_n \tag{4.14}$$

$$G_{l,n} = g_l\, d_n \pi\, l_n, \tag{4.15}$$

where E_{Na} and E_l are the sodium and the leakage equilibrium potentials caused by different ionic concentrations at the inside and outside of the fiber.
$G_{Na,n}$ and $G_{l,n}$ are sodium channel and leakage channel conductances, g_{Na} and g_l the corresponding maximum conductivities per square unit area.
m and h are probabilities (with values between 0 and 1) that reduce the maximum conductance of sodium and leakage channels:

$$\frac{dm}{dt} = [\alpha_m(1-m) - \beta_m m]\, k \tag{4.16}$$

$$= [-(\alpha_m + \beta_m)m + \alpha_m]\, k \tag{4.17}$$

$$\frac{dh}{dt} = [\alpha_h(1-h) - \beta_h h]\, k \tag{4.18}$$

$$= [-(\alpha_h + \beta_h)h + \alpha_h]\, k \tag{4.19}$$

$$k = 3^{0.1T-3.7} \tag{4.20}$$

$$\alpha_m = \frac{97 + 0.363V}{1 + exp\left(\frac{31-V}{5.3}\right)} \qquad \beta_m = \frac{\alpha_m}{exp\left(\frac{V-23.8}{4.17}\right)} \tag{4.21}$$

$$\alpha_h = \frac{\beta_h}{exp\left(\frac{V-5.5}{5}\right)} \qquad \beta_h = \frac{15.6}{1 + exp\left(\frac{24-V}{10}\right)} \tag{4.22}$$

α and β are voltage dependent variables fitted from experimental data to quantify the ion channel kinetics, k is a temperature coefficient which accelerates the gating process for temperatures higher than the original experimental temperature of 37°C, temperature T in °C. The initial conditions of the differential equation system are:

$$V(0) = 0 \tag{4.23}$$

$$m(0) = 0.003 \tag{4.24}$$

$$h(0) = 0.75 \tag{4.25}$$

The nerve fiber model including CRRSS ion channel dynamics at the nodes was implemented using MATLAB. M-files were created to analyze the excitability of the target fibers (Appendix A). A multistep solver based on numerical differentiation formulae was used to compute the solution of the differential equations. Rectangular monophasic stimuli with a pulse width of 1ms are applied in 1V increments, until APs are initiated in the simulated neurons and are able to propagate along the fiber.

4.3. Parameter Values used in the Simulations

Param.	Description	Value	Unit	Ref.
D	Fiber diameter (incl. myelin sheath)	$20 \cdot 10^{-4}$	cm	[Brown 1981]
d	Axon diameter	$0.64\,D$	cm	[Rattay et al. 2000]
l_n	Node length	$1.5 \cdot 10^{-4}$	cm	[Rattay et al. 2000]
	Internode length	$100\,D$	cm	[Rattay et al. 2000]
c_m	Specific membrane capacity	1	$\mu F/cm^2$	[Rattay 1999]
ρ_a	Axoplasmatic resistivity	0.07	$k\Omega\,cm$	[Struijk et al. 1992]
g_m	Membrane conductivity, passive	1	mS/cm^2	[Rattay 1999]
N	Number of myelin sheath layers	$75 \cdot 10^4\,D$	1	
g_{Na}	Sodium channel conductivity	1445	mS/cm^2	[Sweeney et al. 1987]
g_l	Leak channel conductivity	128	mS/cm^2	[Sweeney et al. 1987]
E_{Na}	Equilibrium potential for sodium channels	115	mV	[Sweeney et al. 1987]
E_l	Equilibrium potential for leakage channels	-0.01	mV	[Sweeney et al. 1987]

Table 4.1.: Model parameters. $c_m = 1$ is assumed in the simulations since higher values (e.g. $c_m = 2.5$ as used in [Sweeney et al. 1987]) result in enormous minima and maxima of the activating function after N is adjusted to obtain appropriate propagation velocities for the fibers.

5. Results

In this chapter the excitability of spinal root fibers is analyzed using different stimulation techniques. Representative standard trajectories for dorsal and ventral root fibers are defined in section 5.1. The responses of these roots to imposed electric fields using surface electrodes (tSCS) are presented in section 5.2. The effects of modifications to the VC model geometry on root fiber excitability are investigated in section 5.3. The last section 5.4.2 focuses on the comparison of the excitation of spinal roots using an implanted electrode (eSCS) with the results of tSCS (Section 5.2).

5.1. Standard Geometry of Simulated Root Fibers

Five afferent dorsal root fibers and five efferent ventral root fibers, originating from the lower spinal cord, are simulated in this study. Their standard trajectories whithin the 3D volume conductor model are determined using several anatomical studies. Root fiber identification in anatomical transverse sections at several intervertebral levels [Wall et al. 1990, Cohen et al. 1991] (Figure 2.9) are combined with geometrical measurements [Hasegawa et al. 1996, Lang 1984]. The main features of the simulated lumbar and sacral root fibers are (Figures 5.1 and 5.3):

- strong curvatures at the entry of the fibers into the spinal cord and at their exit of the spinal canal, and
- a long vertical portion inbetween.

For each spinal cord segment from L2 to S1 one dorsal and one ventral root fiber are defined. From their origin within the grey matter to the termination, 18-21mm beyond their exit from the spinal canal below the corresponding vertebrae, the fibers measure between 12.2cm (L2 ventral root fiber) and 19.3cm (S1 dorsal root fiber).

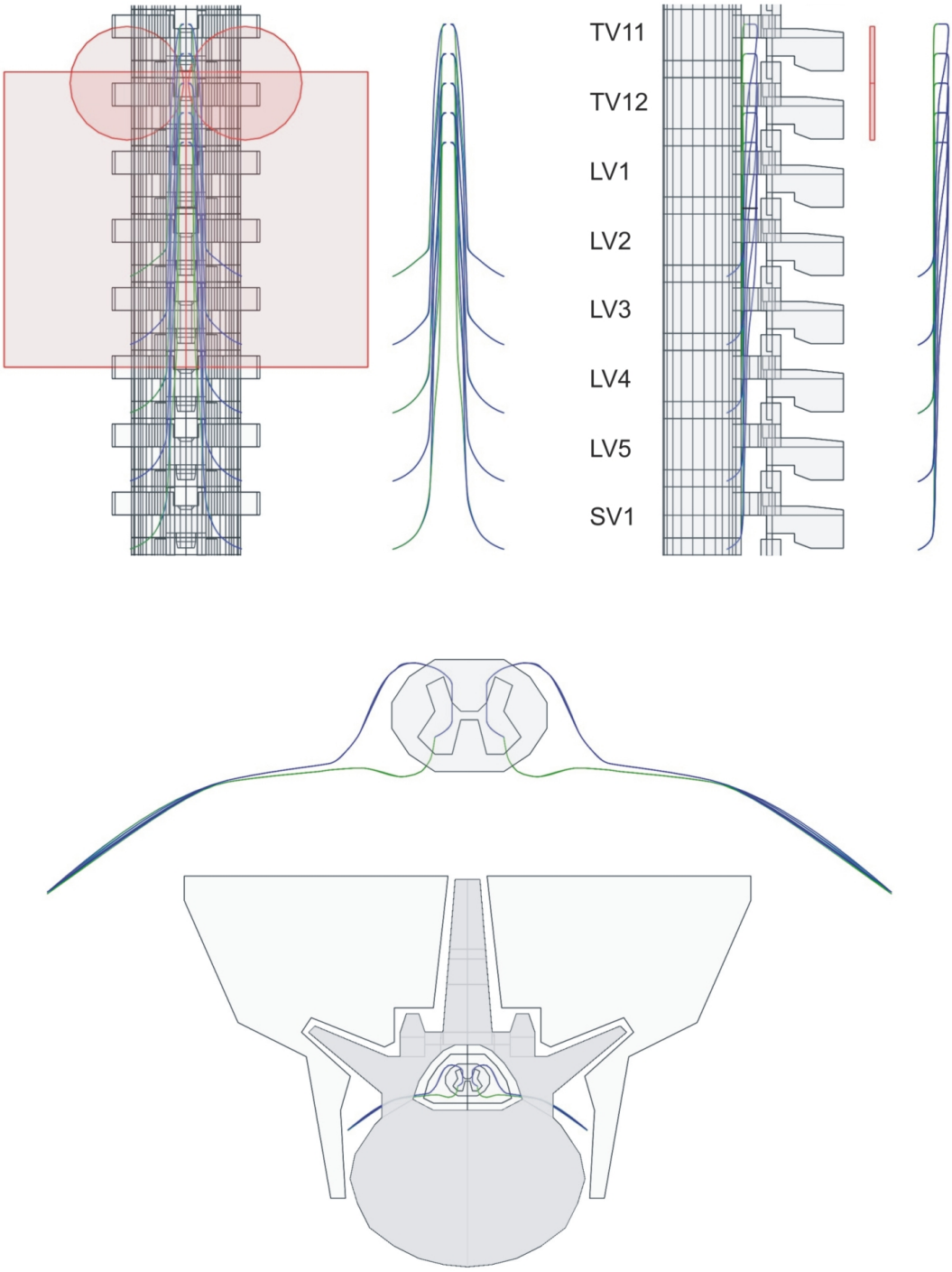

Figure 5.1.: Anatomical structures and electrodes from the VC model including spinal root fibers. Top left: Spine and electrodes (red) from VC model including 5 pairs of dorsal root fibers (blue) and 5 pairs of ventral root fibers (green), view from the back. Top right: Spine and stimulating electrode with root fibers, lateral view. Bottom: Cross section of spine, spinal cord and paraspinal muscles including root fibers, view from the top.

The entry levels of the root fibers into the spinal cord are chosen according to a segment arrangement model based on fiber identification in several cross sections [Wall et al. 1990, Minassian 2000, Rattay et al. 2000] (Figure 2.10), and, considering the position of the stimulating electrode, which is placed over the T11 and T12 vertebral processes as in [Minassian et al. 2007a, Hofstoetter et al. 2008]. The L4 fibers enter the spinal cord at the longitudinal center of the electrode, the entry levels of the L3 and the L2 fibers are 13mm and 26mm higher, whereas the L5 and the S1 fibers enter the spinal cord 13mm and 26mm below (Figure 5.2).

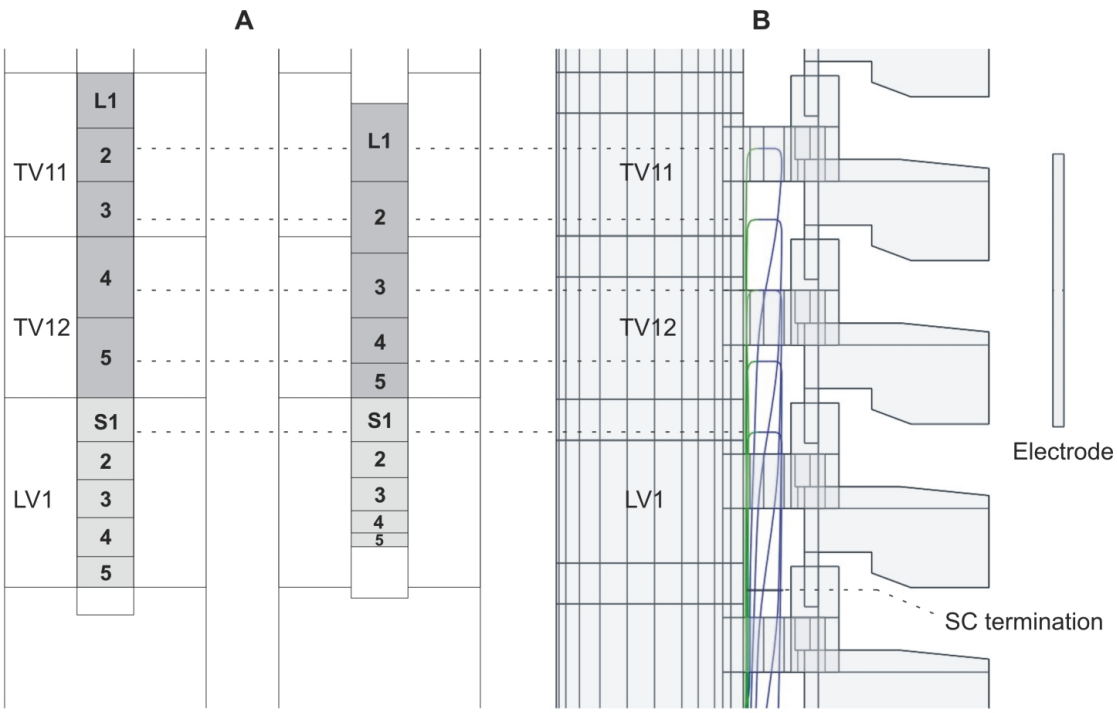

Figure 5.2.: Entry levels of the simulated standard fibers with respect to spinal cord segments. A shows two opposing models of spinal cord segment arrangement derived from [Wall et al. 1990] (left), and [Lang and Geisel 1983] respectively (right), compare Figure 2.10. In B the dorsal root fibers (blue) and the ventral root fibers (green) simulated in this study are depicted together with the spine from a lateral view.

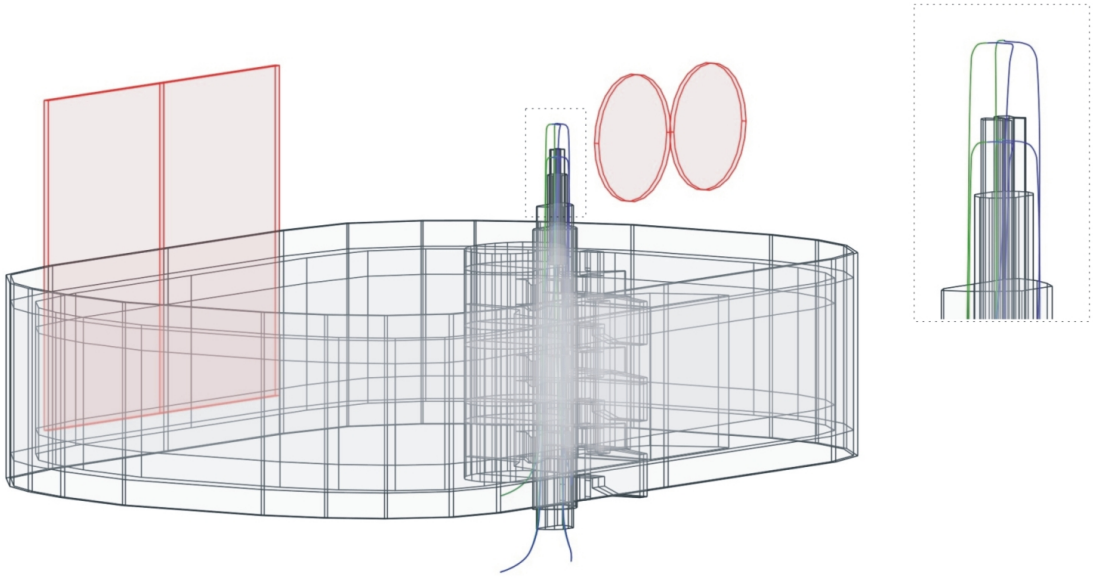

Figure 5.3.: VC model layers with 2 pairs of DR fibers (blue) and VR fibers (green).

5.2. Extracellular Voltage Profiles and Excitation Thresholds of Spinal Root Fibers

The calculated potential distribution from the volume conductor model (Chapter 3) is evaluated along the standard fibers specified in the previous section 5.1. Subsequently, the impact of the imposed electric field on these fibers is analyzed using the nerve fiber model introduced in Chapter 4. Excitation thresholds of the fibers are determined by increasing the stimulus in the nerve fiber model in 1V steps, until action potentials are initiated and are able to propagate along the fiber.

In a first approach, single rectangular stimuli with a pulse width of 1ms are applied with the stimulating electrode on the back being the cathode. To obtain the lowest threshold values, fibers with the largest diameters ($D = 20\mu m$) are simulated. Figure 5.4 shows the excitation of five dorsal root fibers stimulated with the individual threshold voltages (Table 5.1). The potential distribution along corresponding left and right target fibers is identical because of the symmetry about the midsagittal plane, therefore only one side is regarded. For each fiber L2a - S1a (a stands for afferent), the relationship between extracellular voltage V_e (green), activating function (red), and membrane voltage (right) are demonstrated, where each line of the membrane voltage plot shows the temporal course of the potential at each node of Ranvier. V_e and activating function are displayed as functions of the fiber length coordinate.

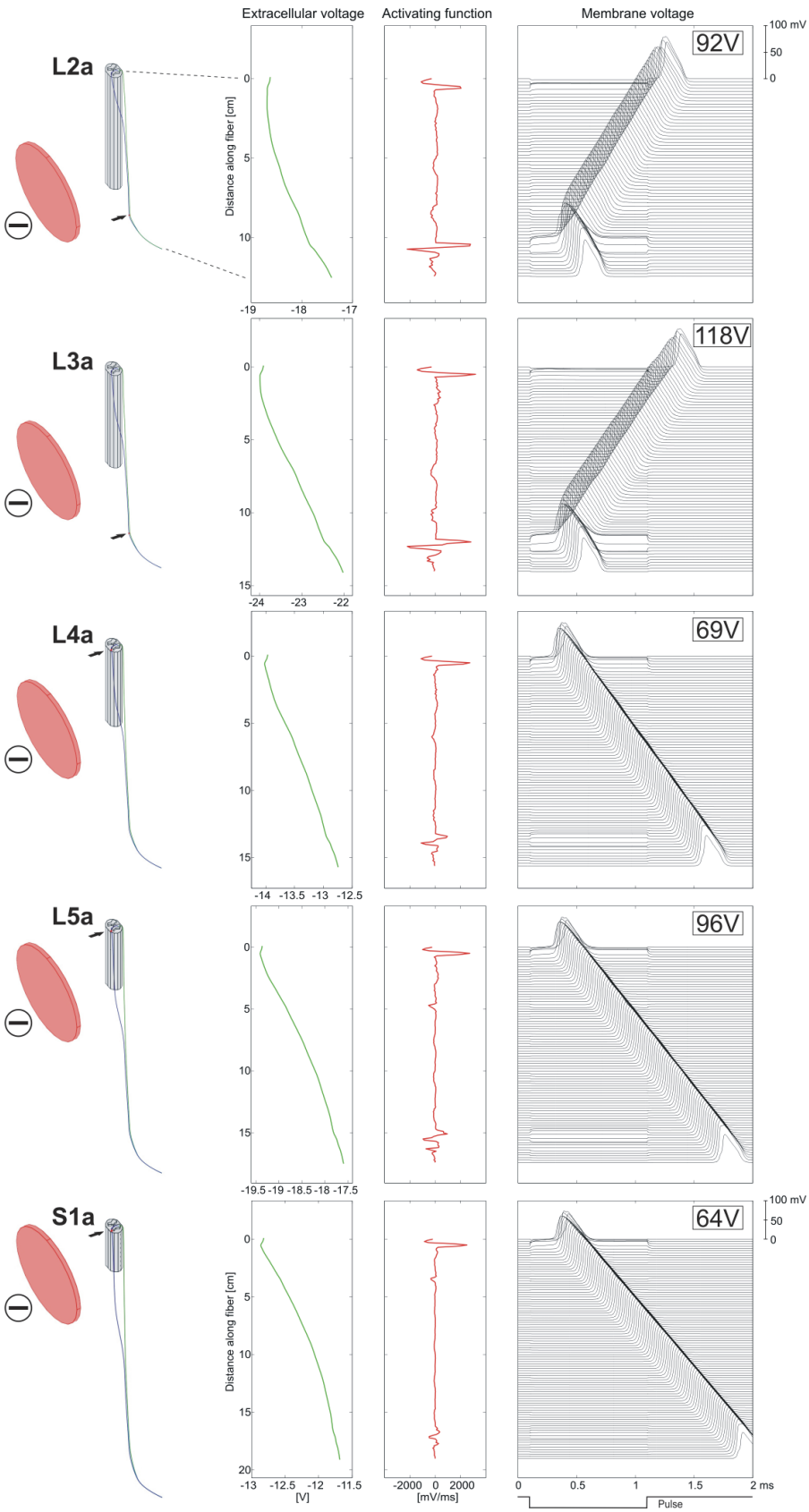

Figure 5.4.: Extracellular voltage, activating function and membrane voltage of dorsal root fibers L2a - S1a, stimulated with a single negative rectangular pulse at threshold voltage.

As mentioned in Section 4.1, the activating function represents the temporal membrane voltage change at stimulus onset, i.e. it defines the slope in each curve of the membrane voltage plot at the beginning of the stimulating pulse. Consequently the maxima of the activating function indicate the sites of spike initiation for stimulation above threshold. In Figure 5.4 arrows and red dots mark these sites on the fibers (left). A red dot localizes the node along the fiber at which an AP is initiated. Note that the electrode position in the images on the left side does not change, instead, the spinal cord is cut off at the different entry levels of the root fibers.

According to the assumptions of constant fiber diameter and constant internode lengths, the value of the activating function is related to the curvature of the extracellular voltage profile along the fiber. For each target fiber, a strong curvature of V_e is visible close to the fiber origin, caused by the curvature of the fiber and by the change of electrical conductivity at spinal cord entry, where the fiber passes the border between the white matter and the well-conducting cerebrospinal fluid. The fibers L4a - S1a are most easily excited at these sites. Another curvature of V_e common to all root fibers can be seen closer to the fiber termination. It is caused by the curvature of the fiber and by the change of electrical conductivity (cerebrospinal fluid - epidural fat) at its exit of the spinal canal. Particularly, for the fibers L2a and L3a this second curvature of the extracellular voltage is more significant for two reasons: (i) These fibers exit the spinal canal closer to the stimulating electrode compared to more caudally originating fibers, and (ii) the angle in which they exit the spinal canal is shorter [Lang 1984], i.e. L2a and L3a fibers have a stronger curvature in these areas compared to L4a, L5a, or S1a fibers. This explains why the fibers L2a and L3a initiate action potentials most likely at their exit of the spinal canal.

The threshold voltages of the fibers L2a, L3a, and L5a are comparatively high (Figure 5.4, Table 5.1), which is caused by the fact that the zones where these fibers enter the spinal cord are located directly ventral to the spinous processes of vertebrae T11 and T12, see Figure 5.1. This means, their primary potential spike initiation areas are dorsally blocked by bone.

In Figure 5.5 the excitation of the ventral root fibers L2e, L3e, and L4e (e stands for efferent) at threshold voltage is presented. L5e and S1e are omitted because these ventral roots could not be excited with voltages lower than 200V. With the stimulating electrode being the cathode, the fibers are most easily excited at the exit of the spinal canal where corresponding dorsal and ventral root fibers show a comparable curvature.

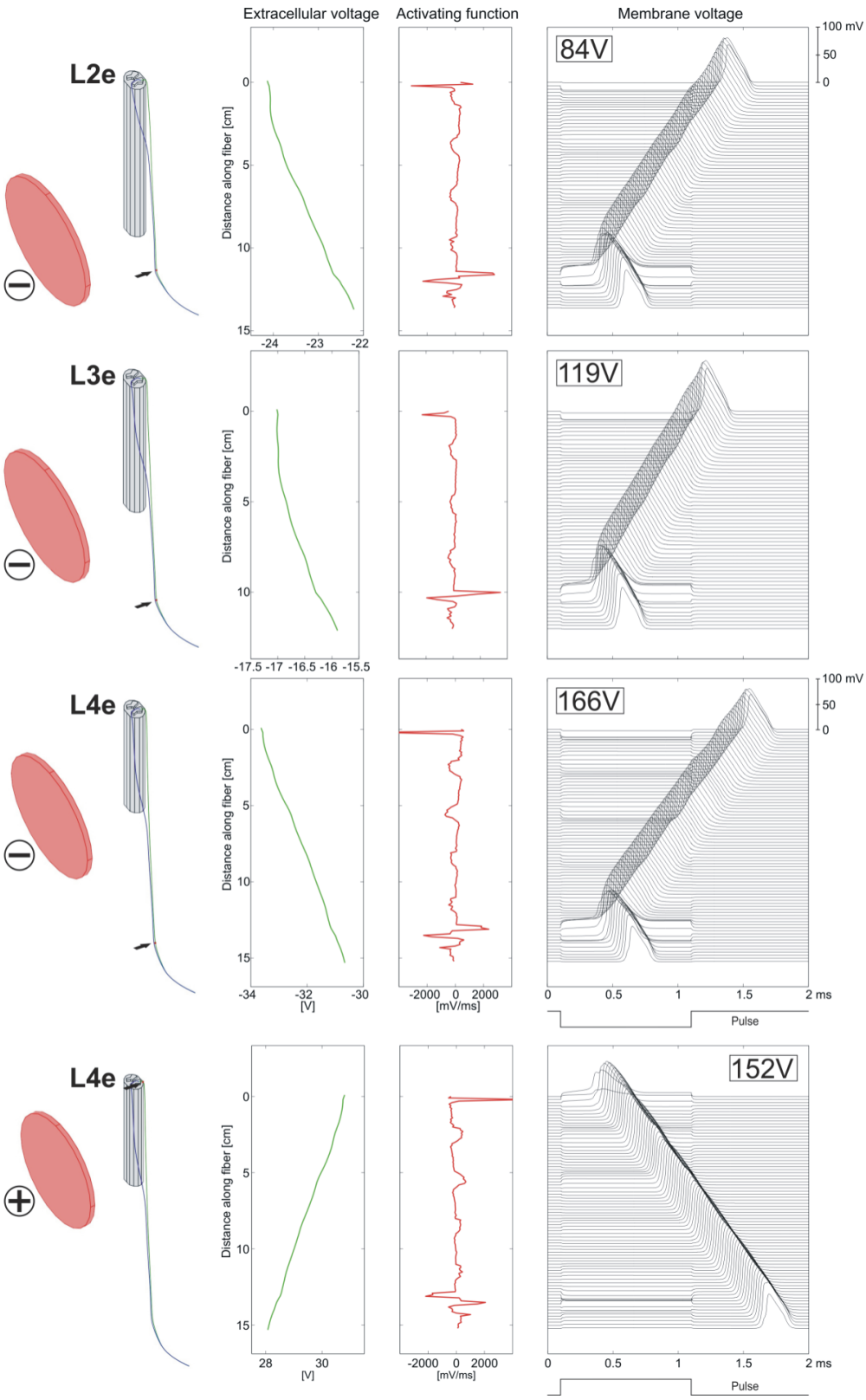

Figure 5.5.: Extracellular voltage, activating function and membrane voltage of ventral root fibers L2e - L4e. The stimuli are single positive (+), and negative rectangular pulses (−) at threshold voltage (indicated in the membrane voltage plots). Arrows and red dots mark the sites of spike initiation along the fibers (left).

The L4e fiber can be excited most easily with a positive stimulating current, initiating an action potential where the fiber enters the spinal cord (bottom of Figure 5.5). The voltage profile and the activating function along L4e are mirrored compared to the situation when a negative pulse is applied.

Figure 5.6 compares the extracellular voltages of all dorsal root fibers (left), and of all ventral root fibers (right). Both fiber groups are stimulated with the lowest threshold voltages within each group, which are 64V for the afferent roots and 84V for the efferent roots, respectively. The similarities and differences of V_e along dorsal and ventral fibers are presented. Corresponding dorsal and ventral fibers show a comparable curvature at their exit of the spinal canal. At the spinal cord entries of the dorsal fibers strong convex curvatures are visible (left plot of Fig. 5.6), whereas weaker concave curvatures are shown at the corresponding positions along the ventral fibers (right plot).

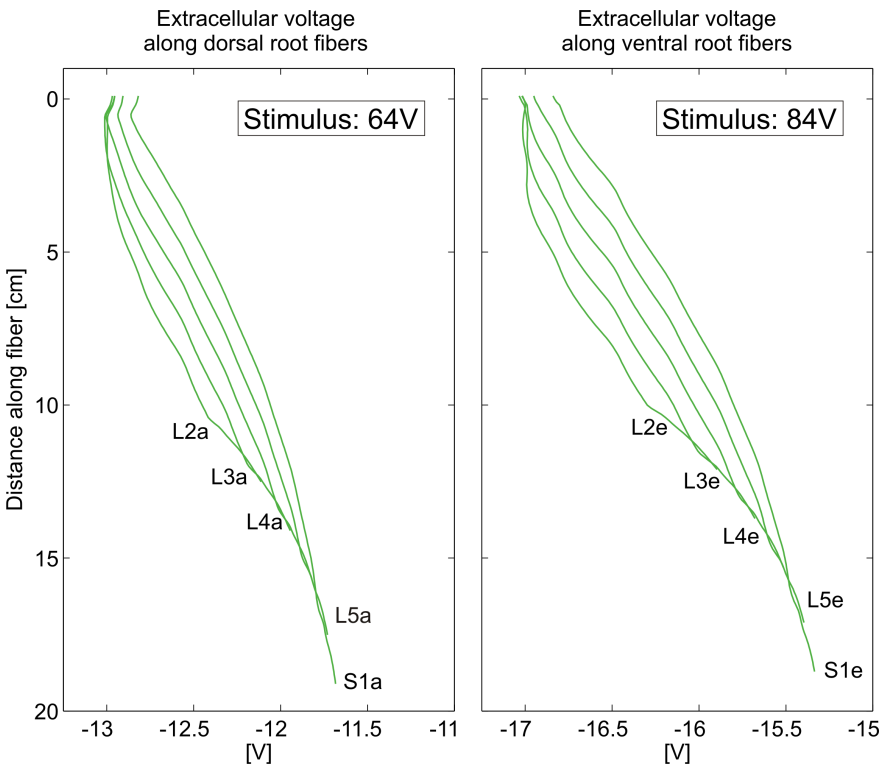

Figure 5.6.: Extracellular voltage profiles of dorsal root fibers (left), stimulated with a negative, rectangular pulse at 64V (lowest threshold voltage among DR fibers), and of ventral root fibers (right), which are stimulated with 84V (lowest threshold voltage among VR fibers). a means afferent fiber (=dorsal root fiber) and e efferent fiber (=ventral root fiber). Pulse width is 1ms.

In Table 5.1 the threshold voltages are listed for each fiber, dependent on the stimulus pulse shape. The effects of positive, and negative rectangular monophasic impulses, and of symmetric biphasic impulses, as used in the stimulation setups of [Minassian et al. 2007a] and [Hofstoetter et al. 2008], are demonstrated. All fibers except for the ventral L4 fiber are more easily excitable using negative (the stimulating electrode being the cathode) instead of positive rectangular stimuli. Applying a biphasic pulse with a positive first phase and a negative second phase of same amplitude to these fibers decreases the threshold voltage on average by 4.7%. Fiber L4e is most easily excited using a biphasic stimulus of opposite polarity (positive second phase), with a threshold being 4.6% lower compared to the use of a positive monophasic pulse. Compared to clinical data [Minassian et al. 2007a, Hofstoetter et al. 2008] the presented threshold values are high, which is discussed in Section 6.3.

Fiber	**Stimulus**			
	Monophasic −	Monophasic +	Biphasic −+	Biphasic +−
L2a	92	–	92	88
L3a	118	–	118	112
L4a	69	–	69	66
L5a	96	–	96	91
S1a	64	–	64	61
L2e	84	138	84	80
L3e	119	194	119	114
L4e	166	152	145	152
L5e	–	–	–	–
S1e	–	–	–	–

Table 5.1.: Threshold voltages of spinal root fibers for different stimulus pulse shapes. Voltages are given in Volt and are omitted if > 200V. Thresholds are calculated for the largest diameter spinal root fibers ($D = 20\mu m$).

Summarizing, excitation of spinal root fibers using surface electrodes is feasible. Large-diameter dorsal root fibers are the primary target structures in transcutanous spinal cord stimulation. The 'hot spot' (= AP initiation site) of each root fiber is located either at its entry into the spinal cord or at its exit from the spinal canal, depending on the distance to the stimulating electrode and on electrode polarity. These two sites are each characterized by (i) a strong curvature of the root fiber, and (ii) a change of electrical conductivity (white matter - cerebrospinal fluid - epidural fat).

Furthermore, the excitability of root fibers is strongly influenced by their spinal cord entry level with respect to the spinous processes of the surrounding vertebrae.

5.3. Modifications of the VC Model Geometry - Effects on Extracellular Voltage and Excitation Thresholds of Spinal Root Fibers

In this section the geometry of the volume conductor model introduced in 3.3.1 is modified in three separate ways and the effects on root fiber excitation are quantified (5.3.1, 5.3.2, and 5.3.3, Figure 5.8):

- Two prismatic volumes are attached to the top and the bottom of the model, with Neumann boundary conditions assigned to the external surfaces and a conductivity value as used for the thorax (compare 3.3.3 and 3.3.2). This is done to reduce the error when assuming Neumann conditions at the top and the bottom cross sections of the model.

- A liver compartment is included within the thorax since it is a large organ located ventrolateral to the spinal cord in the region of interest with a considerably lower conductivity than the mean value assumed for the thorax compartment.

- The aorta is considered as a model enhancement because of its proximity to the spine and its high conductivity compared to the thorax mean value (Figure 5.7).

Figure 5.7.: Cross section image of human anatomy at vertebral level T10.

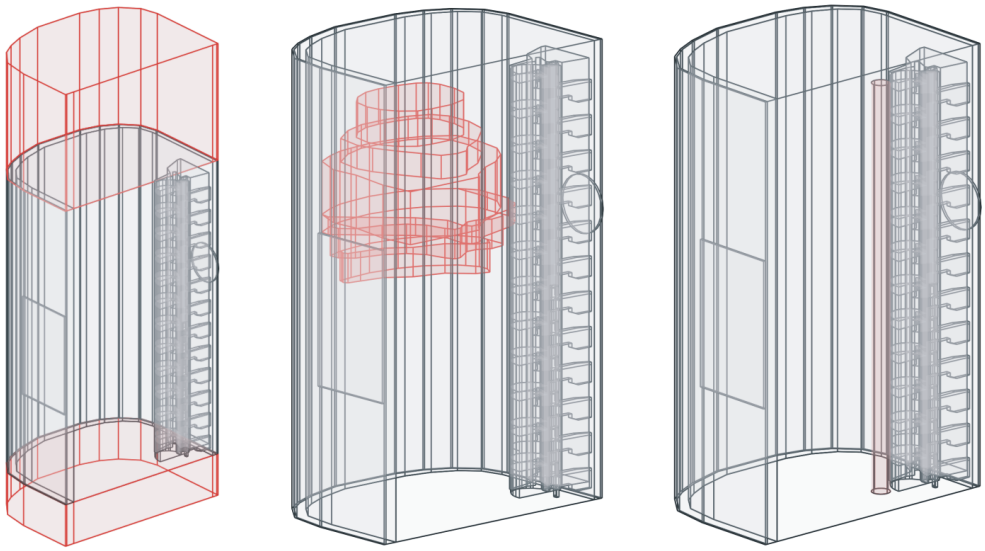

Figure 5.8.: VC model geometry enhancements (red). Left: Extended model with two prismatic volumes on top and bottom. Middle: Liver compartment included within thorax. Right: VC model including aorta compartment.

5.3.1. VC Model Extension

The dimensions of the compartments added on top and bottom of the model are chosen such that the model measures 60cm total in length, and the position of the stimulating electrode is in the longitudinal center of the model. The conductivity of the two additional compartments is 0.25S/m, which yields an overall impedance of 745Ω for the model. The mesh of the 3D model consists of 516616 elements, connected by 100677 nodes. The influence of this volume conductor model extension on the external voltages along several dorsal root fibers is shown in Figure 5.9. The differences regarding activating function and membrane voltage of the L4a fiber when stimulated at threshold voltage are displayed in Figure 5.10. Changes in threshold voltage for each of the simulated fibers are listed in Table 5.2.

The differences in the voltage profiles (Figure 5.9) are marginal and there is practically no change in the activating function shown in Figure 5.10. The threshold voltages increase on average by 3.1% compared to the use of the standard VC model (Table 5.2).

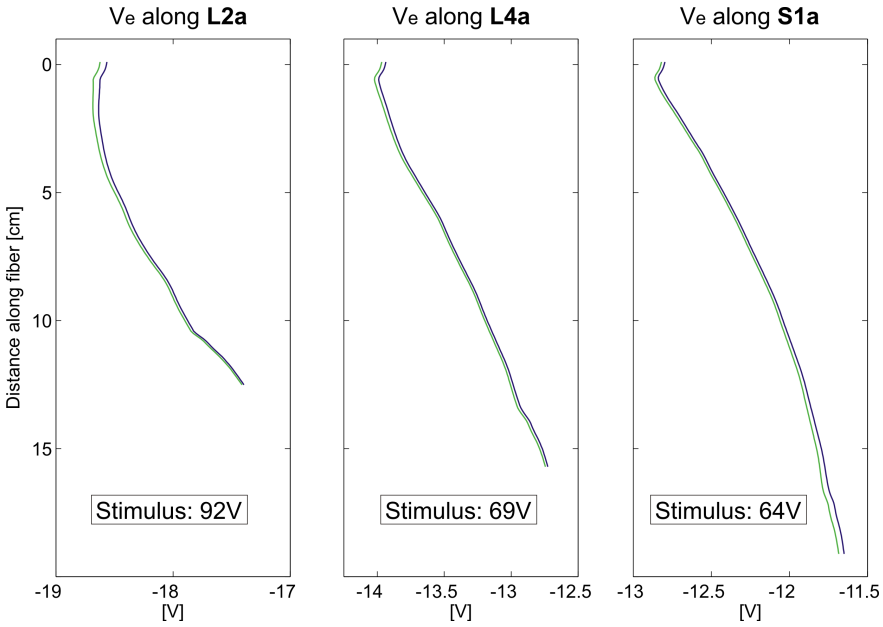

Figure 5.9.: External voltage profiles of dorsal root fibers L2a, L4a, S1a, which are stimulated at threshold voltage (compare Figure 5.4) using the standard VC model (green) and the extended VC model (violet).

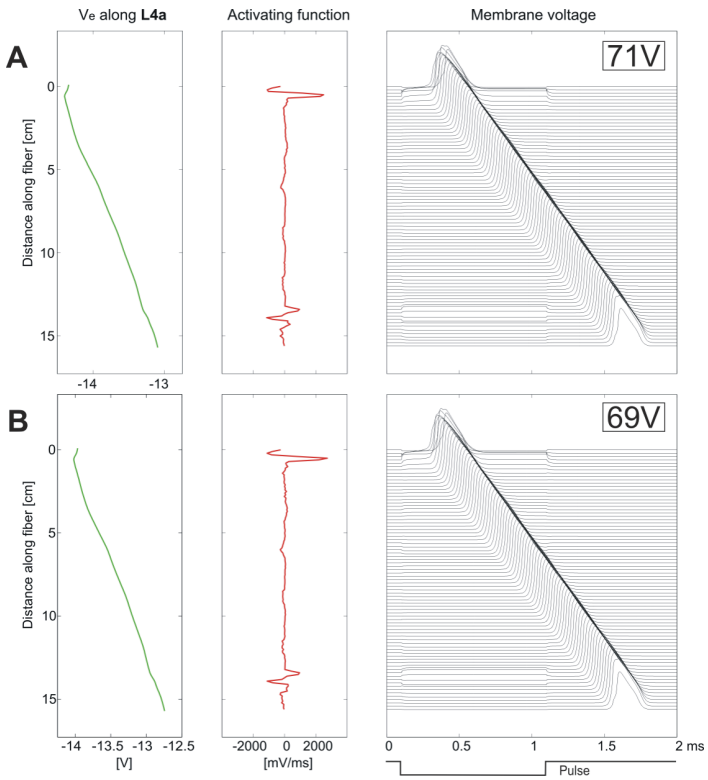

Figure 5.10.: External voltage, activating function, and membrane voltage of the L4a fiber, when stimulated at threshold voltage using the standard VC model (A) and the extended VC model (B).

5.3.2. VC Model including Liver

The liver is implemented in the model by combining several cross sections to form a volume, i.e. the compartment is made up of several prismatic layers. The geometry is taken from an interactive program on the cross-sectional anatomy of the human male based on images of the U.S. NLM 'Visible Human Project' (Figure 5.7).
Since only one half of the body is simulated with Neumann conditions assigned to the sagittal symmetry plane, the results represent a liver compartment in each body half. The conductivity of the liver is 0.13S/m [Foster and Schwan 1989, Gabriel et al. 1996, Miklavcic et al. 2006], which results in a total impedance of 747Ω for the model. The solution is computed at 101433 nodes, connecting 520208 mesh elements. Figure 5.11 shows the effect of this model modification on the external voltages of the fibers L2a, L4a, and S1a. The differences in V_e, activating function and membrane voltage of the L4a fiber stimulated at threshold voltage are presented in Figure 5.12. In Table 5.2 the threshold values of all simulated fibers using the enhanced model are listed.

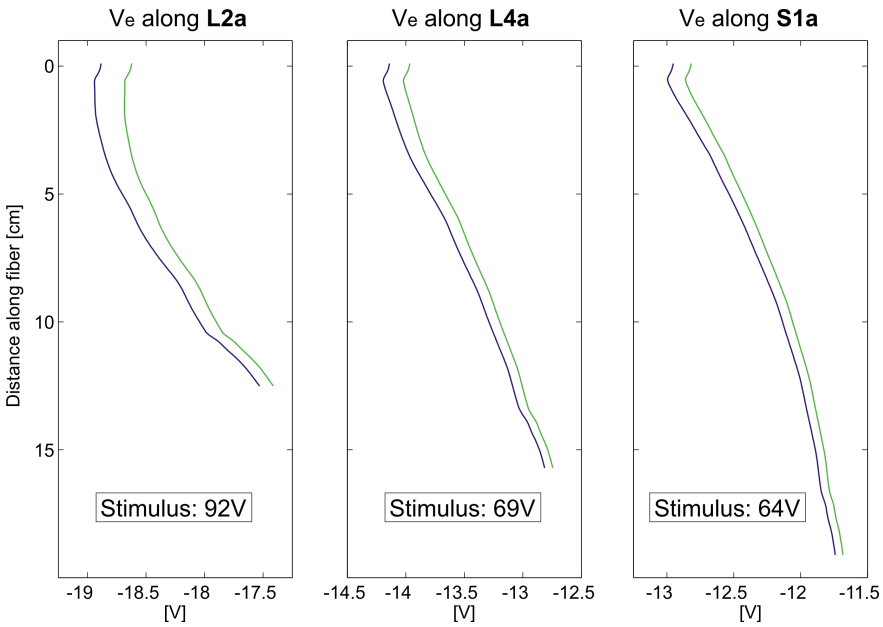

Figure 5.11.: External voltage profiles of dorsal root fibers L2a, L4a, S1a, which are stimulated at threshold voltage (compare Figure 5.4) using the standard VC model (green) and the VC model including a liver compartment (violet).

The presented voltage profiles (Figure 5.11) reveal a small shift of the curves along the x-axis (V), however the shapes of the voltage profiles remain almost unchanged. Activating function and membrane voltage of the fiber L4a show minimal differences in comparison (Figure 5.12). The threshold voltages of the spinal root fibers decrease on average by 4.6% (Table 5.2).

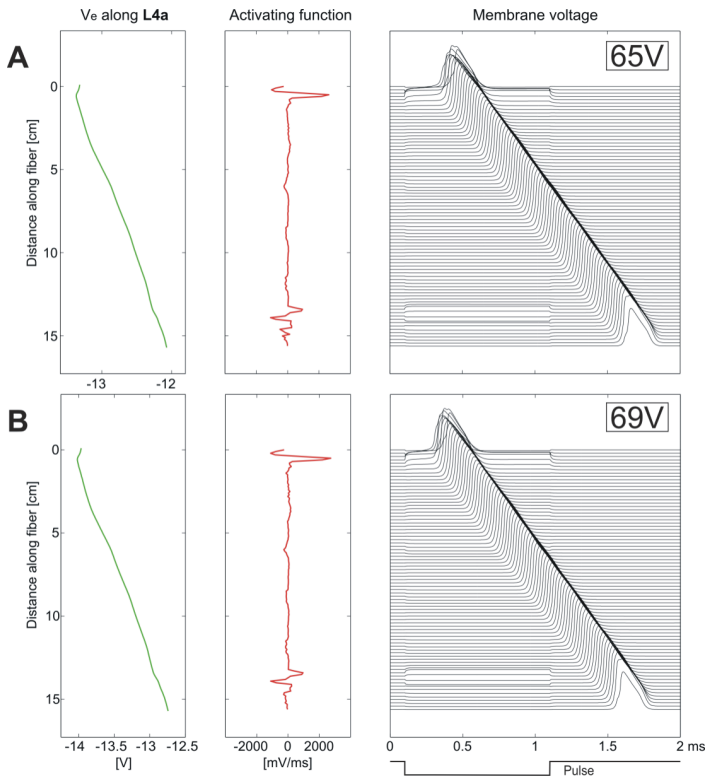

Figure 5.12.: External voltage, activating function, and membrane voltage of the L4a fiber, when stimulated at threshold voltage using the standard VC model (A) and the VC model containing a liver compartment (B).

5.3.3. VC Model including Aorta

The aorta is simulated as a tubular compartment adjacent to the spine. Since the symmetry of the body about the midsagittal plane is utilized, the results represent one aorta in each body half, as in case of the liver (5.3.2). The conductivity of the aorta is 0.68S/m according to [Foster and Schwan 1989, Gabriel et al. 1996, Klepfer et al. 1997, Miklavcic et al. 2006], the overall impedance of the model is 746Ω, which is equal to the value of the standard model. The mesh of the 3D model consists of 515816 elements and 100712 nodes. The effects on the external voltages of L2a, L4a, and S1a are presented in Figure 5.13. The activating function and the membrane voltage of fiber L4a using the enhanced model in comparison with the standard VC model are shown in Figure 5.14. Table 5.2 lists the threshold voltages of the simulated dorsal and ventral root fibers utilizing this modified VC model, compared to the values using the standard VC model and the above mentioned enhanced models.

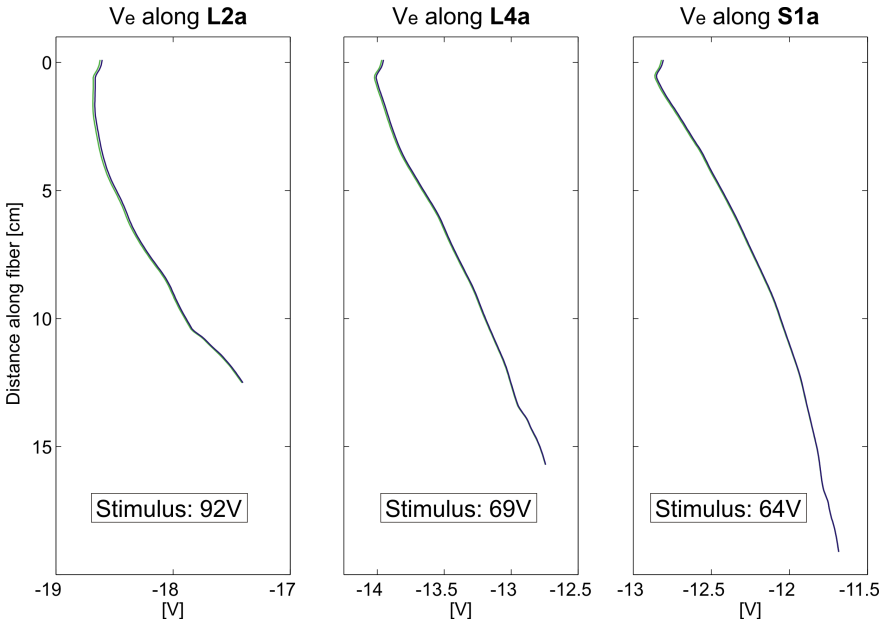

Figure 5.13.: External voltage profiles of dorsal root fibers L2a, L4a, S1a, which are stimulated at threshold voltage (compare Figure 5.4) using the standard VC model (green) and the VC model including an aorta compartment (violet).

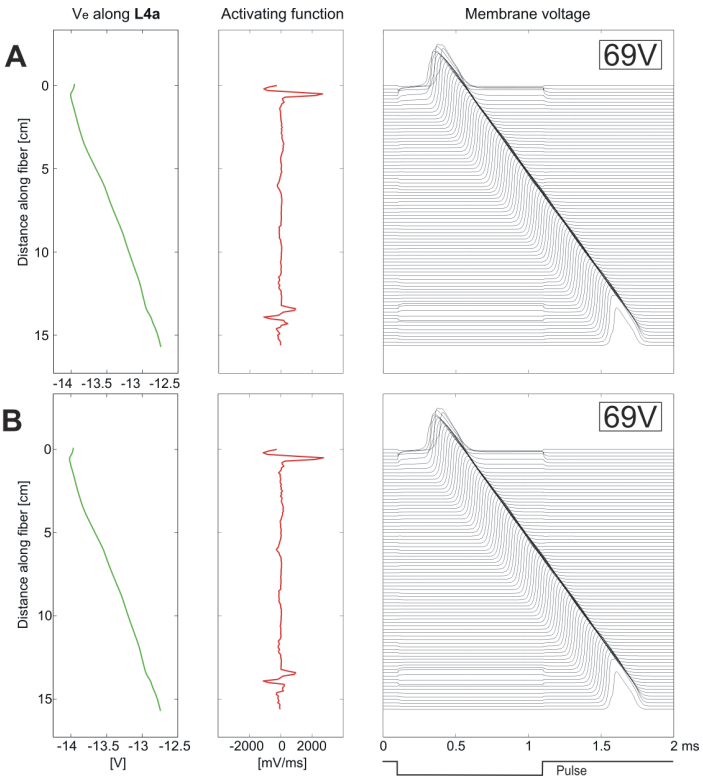

Figure 5.14.: External voltage, activating function, and membrane voltage of the L4a fiber, when stimulated at threshold voltage using the standard VC model (A) and the VC model containing an aorta compartment (B).

The voltage profiles (Figure 5.13) are congruent to a large extent, activating function and membrane voltage of L4a show no difference in comparison with the corresponding curves using the standard VC model (Figure 5.14). The threshold voltages increase on average by 0.7% (Table 5.2).

Fiber	**VC Model**			
	Standard	Extended	Including Liver	Including Aorta
L2a	92	94	88	93
L3a	118	121	113	118
L4a	69	71	65	69
L5a	96	98	89	96
S1a	64	65	61	64
L2e	84	86	81	85
L3e	119	123	115	120
L4e	166	175	159	169
L5e	–	–	–	–
S1e	–	–	–	–

Table 5.2.: Threshold voltages of spinal root fibers using different VC models. A negative rectangular stimulating pulse is applied with pulse width 1ms. Voltages are given in Volt and are omitted if > 200V.

Concluding, the results in this section show that the simplified VC model geometry is appropriate. The influences of including an aorta compartment in the VC model are negligible and the effects of using an extended VC model or a model considering the liver within the thorax compartment are minimal and cancel each other out.

5.4. Comparison with Simulations of Neural Responses using an Implanted Electrode

In this section excitation of spinal root fibers with a single bipolar electrode implanted into the epidural space is simulated (eSCS). The required modifications in the volume conductor model are presented in Section 5.4.1. Subsequently, in Section 5.4.2 the results are displayed (i.e. V_e, activating function, membrane voltage and excitation thresholds of the fibers defined in Section 5.1) and compared with the results from tSCS simulations (Section 5.2).

5.4.1. Implementation of an Implanted Electrode in the VC Model

The VC model geometry described in Section 3.3 is used excluding the surface electrode compartments. The two active contacts of the cylindrical implanted electrode are modeled as boundaries with constant voltages (Dirichlet conditions). The boundaries are created by subtracting the volume representing the electrode from the epidural fat compartment. The geometry of the VC model and the position of the implanted electrode with respect to the anatomical structures and simulated root fibers are presented in Figure 5.15. It is located on the same vertical level (TV11 - TV12) as the stimulating surface electrode in case of transcutaneous stimulation. The electrode measures 30mm in length and 1.27mm in diameter, the active contacts are 3mm long each. These dimensions represent an electrode widely used in clinical application, and are in accordance with [Rattay et al. 2000, Minassian 2000]. Calculations showed that applying Neumann boundary conditions to the top and the bottom cross sections of the model geometry results in a shifted voltage distribution along the fiber pathways, since the electrode is not positioned in the vertical center of the model. The distance of the electrode to the uppermost simulated vertebra is much shorter than to the lowest vertebra in the model. Best results are obtained when Dirichlet boundary conditions with $\mathbf{\Phi} = 0$ Volt are applied to the external top and bottom surfaces.

Note that Dirichlet boundaries have an effect like voltage sources. In multipolar stimulation a net current from the modeled electrode contacts to these boundaries may influence the voltage distribution calculated by the model. To avoid this effect the anodal and cathodal voltages are chosen equal in magnitude. 5V is applied to the upper contact, -5V to the lower contact, representing a potential difference of 10V.

For simulations with any voltage strength or the other polarity, the results calculated by the finite element method are multiplied by the corresponding factor.
The VC model mesh consists of 523197 elements, connected by 99320 nodes at which the solution is computed (Figure 5.16).

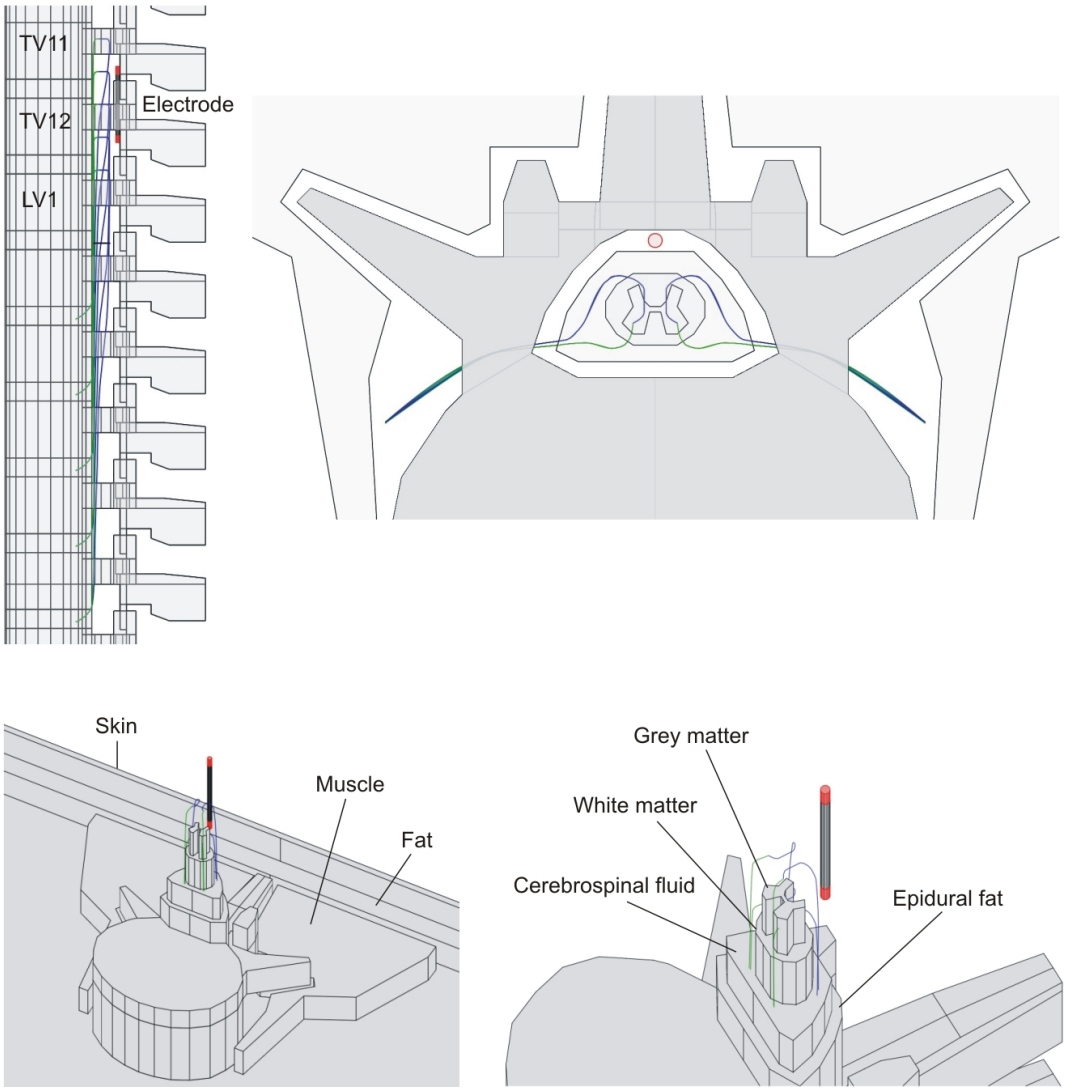

Figure 5.15.: VC model geometry including the position of the implanted electrode. The active contacts of the electrode are highlighted in red, dorsal root fibers are exhibited in blue, ventral roots in green. Top left: Spine and electrode position including root fibers, lateral view. Top right: Cross section of spine, spinal cord and paraspinal muscles including root fibers and electrode position, view from the top. Bottom: Anatomical structures and electrode position, 3D visualization.

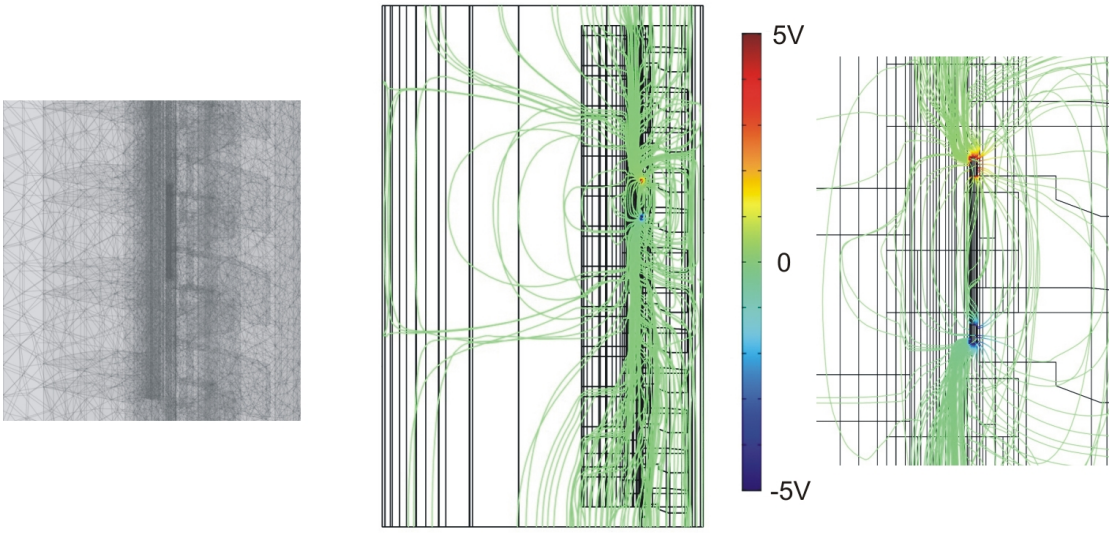

Figure 5.16.: Mesh and solution of the VC model with implanted electrode. Left: 3D representation of the mesh in the region of interest. Middle and right: Calculated total current density, sagittal view. Color code illustrates the electrical potential.

5.4.2. Surface Electrodes (tSCS) versus Implant (eSCS) - Comparison of Spinal Root Fiber Excitation

In the simulations of epidural SCS the proceeding is similar to that of transcutaneous SCS simulations. The effect of the calculated electric field in the VC model 5.4.1 is analyzed using the nerve fiber model introduced in Chapter 4, compare Section 5.2. Excitation thresholds of the fibers are determined by increasing the stimulus in 0.1V steps, until action potentials are initiated and are able to propagate along the fiber. Stimulus pulse widths are $210\mu s$, which is common in eSCS [Rattay et al. 2000]. Figures 5.17 and 5.18 show the excitation of the dorsal root fibers L2a - S1a (with $D = 20\mu m$), which are stimulated at threshold voltage in tSCS (left, compare Figure 5.4) and in eSCS (right) by application of a single rectangular pulse.

V_e, activating function, and membrane voltage of each fiber are displayed to compare the effects of the two stimulation techniques. The polarity of the implanted electrode is u+l−, which means the upper contact is the anode, the lower contact the cathode. Threshold voltages are shown in the membrane voltage plots, and are listed in Table 5.3. Spike initiation sites along the fibers are marked by arrows and red dots.

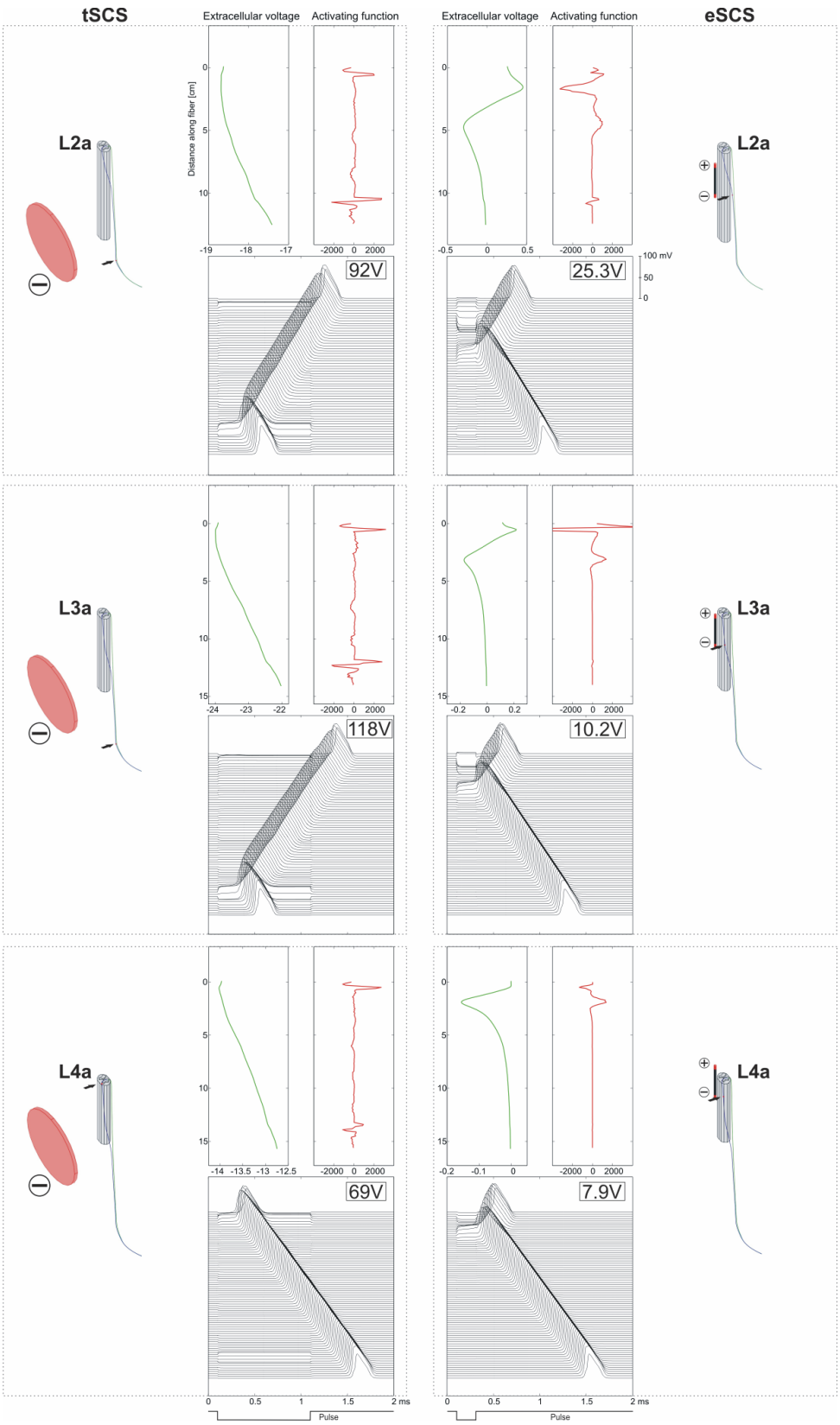

Figure 5.17.: Extracellular voltage, activating function and membrane voltage of DR fibers L2a - L4a, stimulated at threshold voltage with surface electrodes (left) and with an implanted electrode (right).

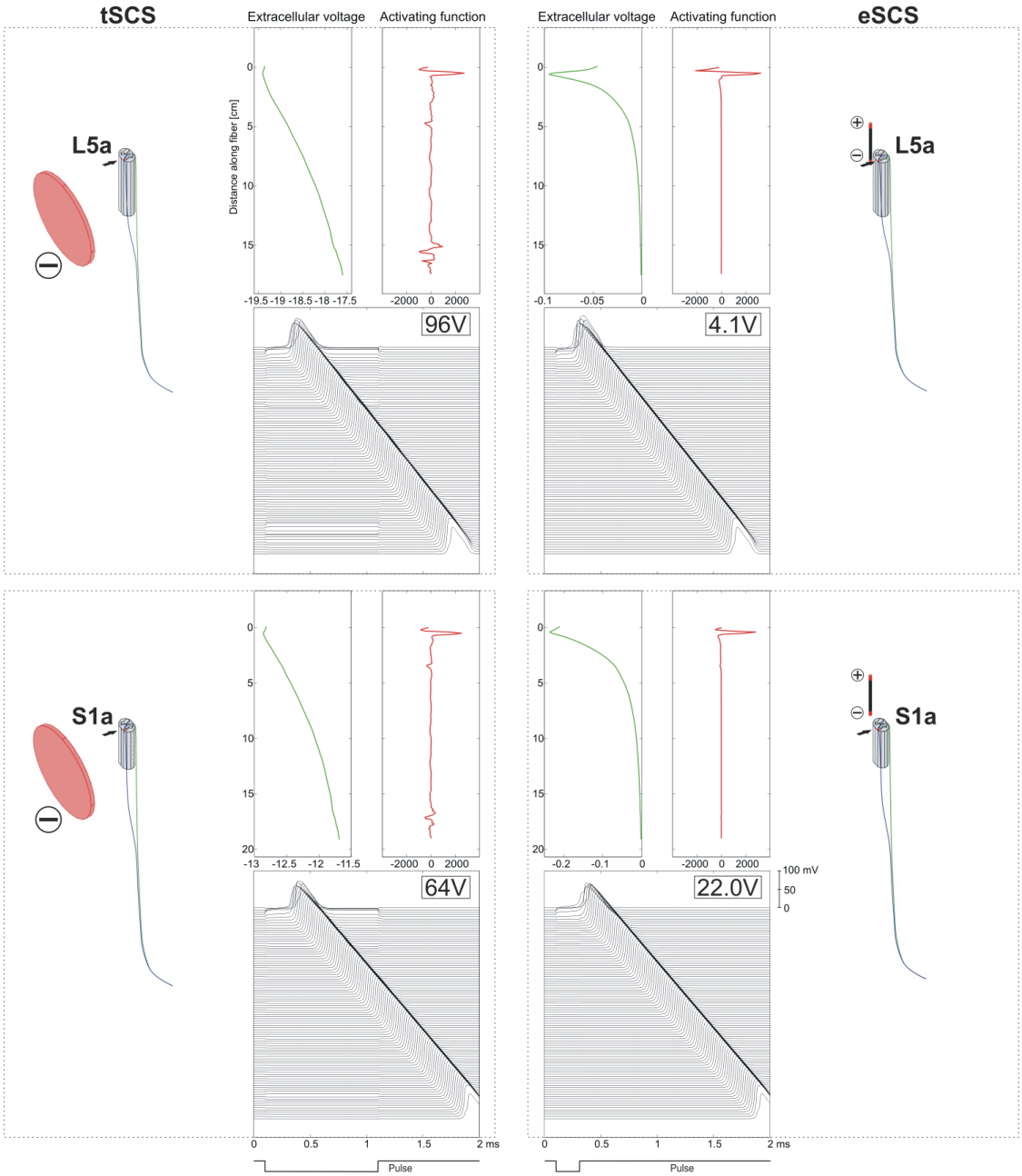

Figure 5.18.: Extracellular voltage, activating function and membrane voltage of DR fibers L5a and S1a, which are stimulated at threshold voltage with surface electrodes (left) and with an implanted electrode (right) by application of a single rectangular pulse.

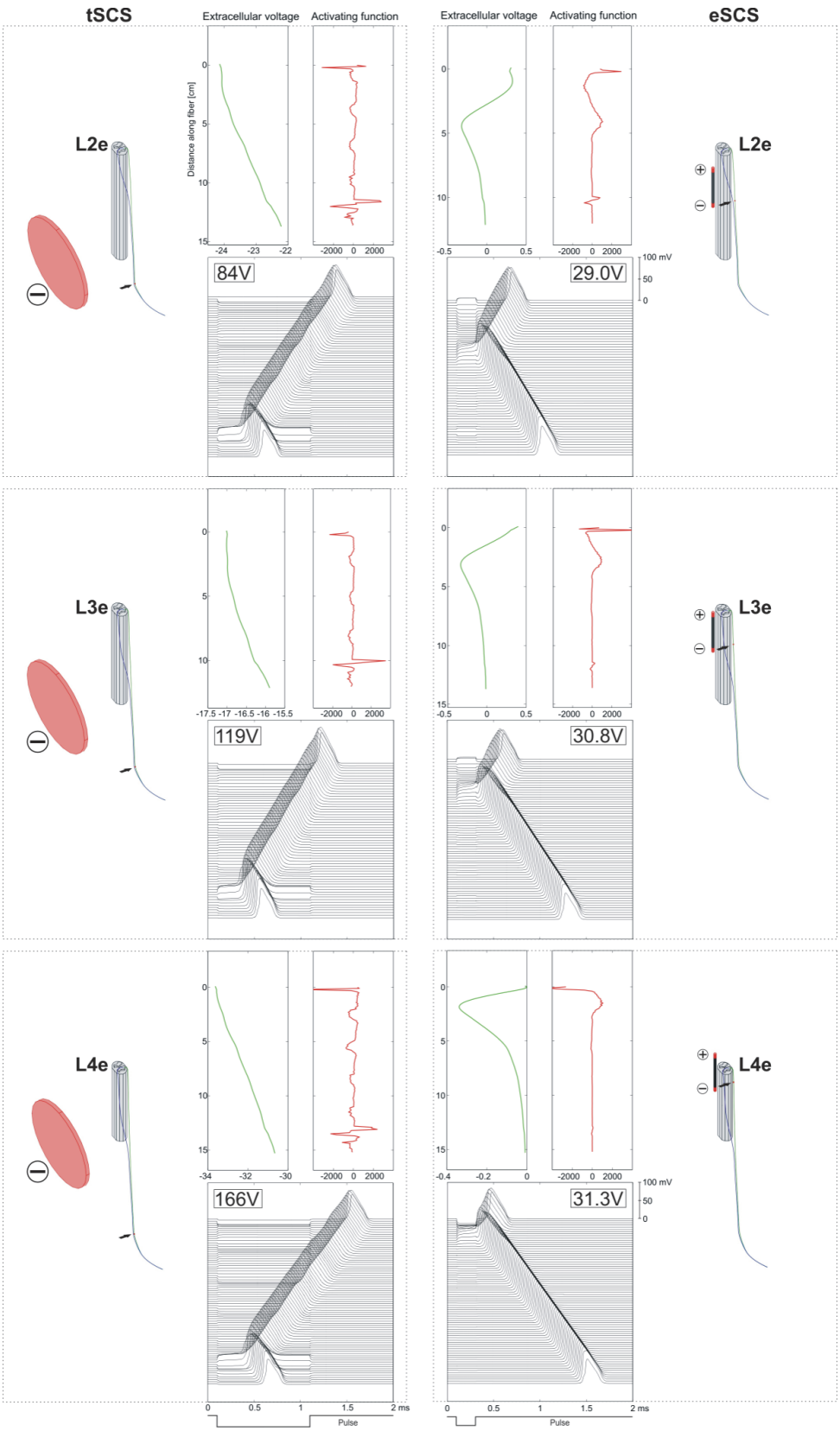

Figure 5.19.: Extracellular voltage, activating function and membrane voltage of VR fibers L2e - L4e, which are stimulated at threshold voltage with surface electrodes (left) and with an implanted electrode (right). Arrows mark AP initiation sites along the fibers.

In Figure 5.19 excitation of the ventral root fibers L2e, L3e, and L4e, stimulated at threshold voltage using surface electrodes (left) and an implanted electrode (right) is presented. L5e and S1e are omitted because these root fibers could not be excited with voltages lower than 200V using surface electrodes. In tSCS the stimulating surface electrode is the anode, in eSCS the electrode polarity is u+l−. In case of epidural stimulation, the AP initiation sites on the fiber trajectories are nodes close to the cathode (compare Figures 5.17 and 5.18).
Figure 5.20 reveals a common spike initiation site on VR fiber L4e in both stimulation methods, with the stimulating surface electrode being the anode and a u−l+ polarity of the implanted electrode. Note that V_e and the activating function are mirrored compared to stimulation with the opposite polarity (Figure 5.19, bottom).

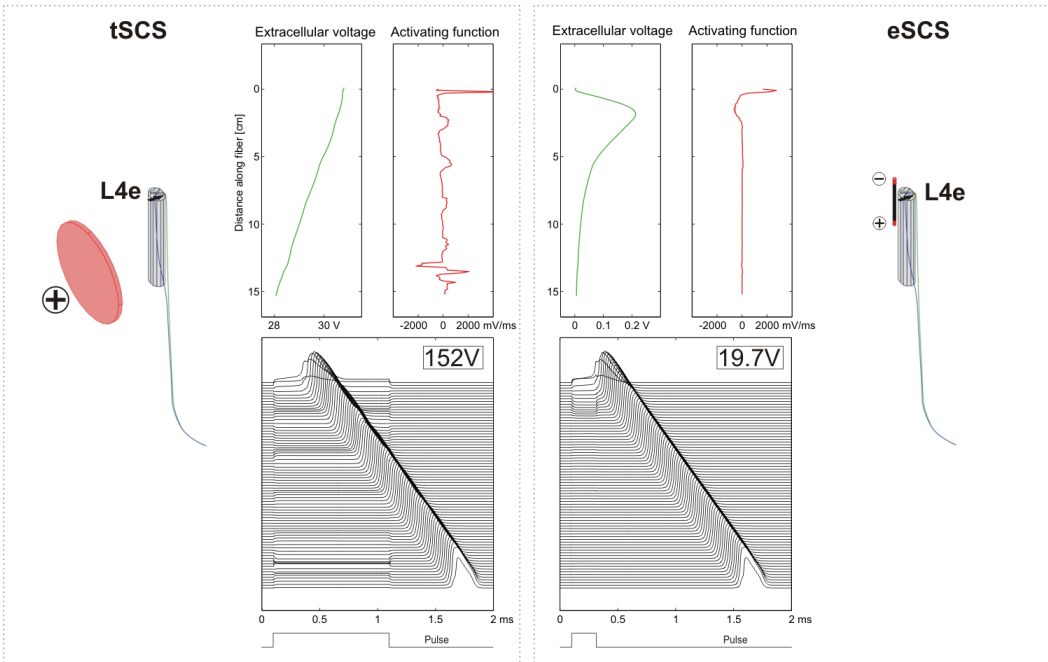

Figure 5.20.: Extracellular voltage, activating function and membrane voltage of fiber L4e, stimulated at threshold voltage with surface electrodes (left) and with an implanted electrode (right). The polarities are opposite compared to Figure 5.19. In tSCS: The stimulating surface electrode is the anode. In eSCS: the upper contact is the cathode, the lower contact the anode.

Figure 5.21 compares the extracellular voltages of all DR fibers (left), and of all VR fibers (right). Both fiber groups are stimulated with the lowest threshold voltages within each group, which are 4.1V for the afferent roots and 29.0V for the efferent roots, using the u+l− polarity and monophasic stimuli (Table 5.3). Corresponding dorsal and ventral fibers show a comparable convex curvature at the level of the cathode.

Concave curvatures are displayed for fibers L2a - L4a, and L2e close to the level of the anode, and for fibers L4e and L5e close to their origin, caused by the curvature of these root fibers at spinal cord entry. In this region along the fiber pathway, a change of electrical conductivity (cerebrospinal fluid - white matter) occurs, which contributes to the excitablility of the fiber (compare [Rattay et al. 2000, Minassian 2000]). When stimulated with the opposite polarity (u−l+) the concave curvatures in V_e become convex, resulting in high values of the activating function and AP initiation in the corresponding regions.

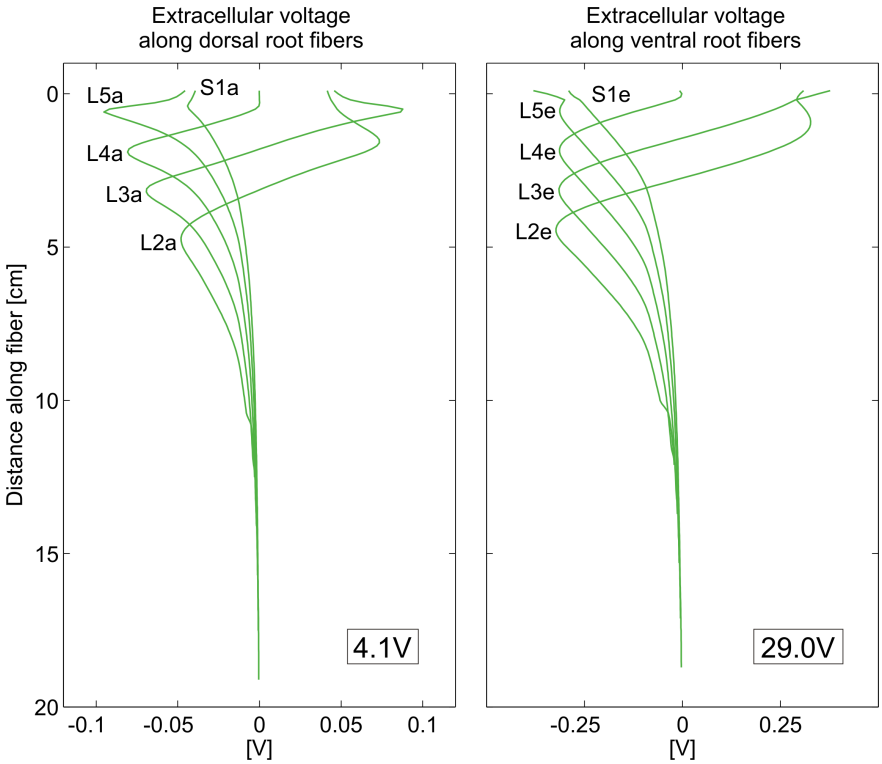

Figure 5.21.: Extracellular voltage profiles of DR fibers (left), stimulated with a single rectangular pulse at 4.1V, and of VR fibers (right), which are stimulated with 29.0V. Electrode polarity is u+l−, pulse width is 210μs. The two applied voltages are the lowest threshold values using the u+l− polarity and monophasic stimuli (Table 5.3).

Figure 5.21 reveals that in epidural stimulation the extracellular voltage profiles of the target fibers are highly influenced by the distance to the active contacts of the electrode (compare [Rattay et al. 2000, Minassian 2000]). The spike initiation sites of the simulated DR fibers are nodes close to the cathode (Figures 5.17, 5.18). Ventral root fibers are excited most easily at nodes close to the cathode, or at their spinal cord entry if close to the anode (Figures 5.19, 5.20). This explains the differences in V_e,

the resulting activating functions and spike initiation sites of fibers L2a - L4a, and the similarities along fibers L5a and S1a, when comparing the results of eSCS and tSCS simulations.

Fiber	**Monophasic stimulus**		**Biphasic stimulus**	
	u+l−	u−l+	u−l+ → u+l−	u+l− → u−l+
L2a	25.3	10.5	10.5	10.0
L3a	10.2	3.8	3.8	3.6
L4a	7.9	12.5	7.6	7.9
L5a	4.1	34.7	3.9	4.1
S1a	22.0	–	21.1	22.0
L2e	29.0	33.1	27.8	29.0
L3e	30.8	–	29.5	30.8
L4e	31.3	19.7	19.7	18.8
L5e	–	14.9	14.9	14.2
S1e	–	–	–	–

Table 5.3.: Threshold voltages of spinal root fibers for different stimuli using an implanted electrode. u means upper contact, l lower contact. In biphasic stimulation the first phase is followed immediately by the second phase. Voltages are given in Volt and are omitted if > 50V. Thresholds are calculated for the largest diameter spinal root fibers ($D = 20\mu m$). Stimulus pulse widths are $210\mu s$.

The threshold voltages in eSCS, dependent on the stimulus pulse shape, are listed for each fiber in Table 5.3. The effects of rectangular monophasic impulses using both polarities, and of symmetric biphasic impulses, are shown. In clinical application of electrical stimulation with implanted electrodes the stimulus signal is always biphasic to avoid charge accumulation in the tissues surrounding the electrode. In every stimulation cycle the second phase is applied for charge compensation. The threshold of fibers which are more easily excitable using the u+l− polarity (L4a - S1a,L2e,L3e) decreases on average by 4.2% when applying a biphasic pulse with the u+l− polarity in the second phase. L2a, L3a, and L4e, L5e are most easily excited using a biphasic stimulus of opposite polarity (u+l− in the first phase), with thresholds being 4.7% lower on average compared to the application of a monophasic impulse.

Comparing the effects of tSCS and eSCS, identical spike initiation sites are shown for DR fibers originating at or below the level of the cathode in eSCS, being the lower contact of the implanted electrode (u+l− polarity), and in tSCS the stimulating

surface electrode is the cathode. Analogous, the excitation of VR fibers originating at or below the level of the anode using a u+l− polarity in eSCS is similar to the excitation of the same fibers in tSCS with the stimulating surface electrode being the anode. The 'hot spots' of these fibers remain unchanged.

Summarizing, comparable excitation patterns of the same target neurons are obtained in both stimulation techniques, either using surface electrodes or implants, depending on electrode position and polarity.

6. Discussion

In this chapter the presented results are interpreted. Section 6.1 focuses on the comparison of excitation patterns for dorsal root fibers in transcutaneous and epidural SCS. In section 6.2 the relation between stimulus strength and recruitment of dorsal root fibers is investigated in consideration of experimental measurements. In the last section 6.3 the limitations of the utilized models are discussed.

6.1. Similarities of Neural Responses in tSCS and eSCS

Spinal root fibers can be excited using an implanted electrode [Rattay et al. 2000, Murg et al. 2000, Pinter et al. 2000] or with surface electrodes [Minassian et al. 2007a, Hofstoetter et al. 2008]. In the previous chapter 5.4.2 similar excitation of root fibers in both stimulation strategies is shown, dependent on the positions and the polarities of the electrodes. In tSCS and in eSCS geometric and electric factors result in 'hot spots' for extracellular electrical excitation at the sites where the fibers enter the spinal cord (Figures 5.18 and 5.20 in Chapter 5) [Rattay et al. 2000]. These low-threshold sites are created by a sudden change of the generated potential distribution along the fibers at the interface between the rootlets and the spinal cord owing to (i) the significant difference in electrical conductivities of the cerebrospinal fluid and the spinal cord [Minassian et al. 2007b], and (ii) the strong curvatures of lumbosacral root fibers as they enter the cord (most likely perpendicular to its surface) [Rattay et al. 2000, Struijk et al. 1993b].
In case of tSCS, additional potential 'hot spots' are the sites where the root fibers exit the spinal canal at the interface between cerebrospinal fluid and epidural fat (Figures 5.4 and 5.5 in chapter 5). In these regions the external voltage along the fibers changes abruptly, caused by the different conductivities of the two mentioned adjacent materials and by the curvature of the roots.

Figure 6.1 shows the results of the simulations for dorsal root fiber S1a when stimulated using surface electrodes (A) and an implant (B). Input data and excitation patterns are displayed for stimulation at threshold voltage. Epidural SCS simulation results from [Rattay et al. 2000] are included for comparison (C). Extracellular voltage, activating function and membrane voltage of a dorsal S1 fiber excited using an implanted electrode are displayed. The shapes of V_e in (B) and (C) are almost identical, the activating function in (C) shows a larger peak at the 'hot spot' of the simulated fiber. This difference can be caused by several factors, as discussed in Section 6.3. When stimulated transcutaneously at threshold voltage an AP is initiated at the same site along the fiber as in case of eSCS, as predicted by the strong curvature in V_e and the peak of the activating function at the corresponding location in (A).

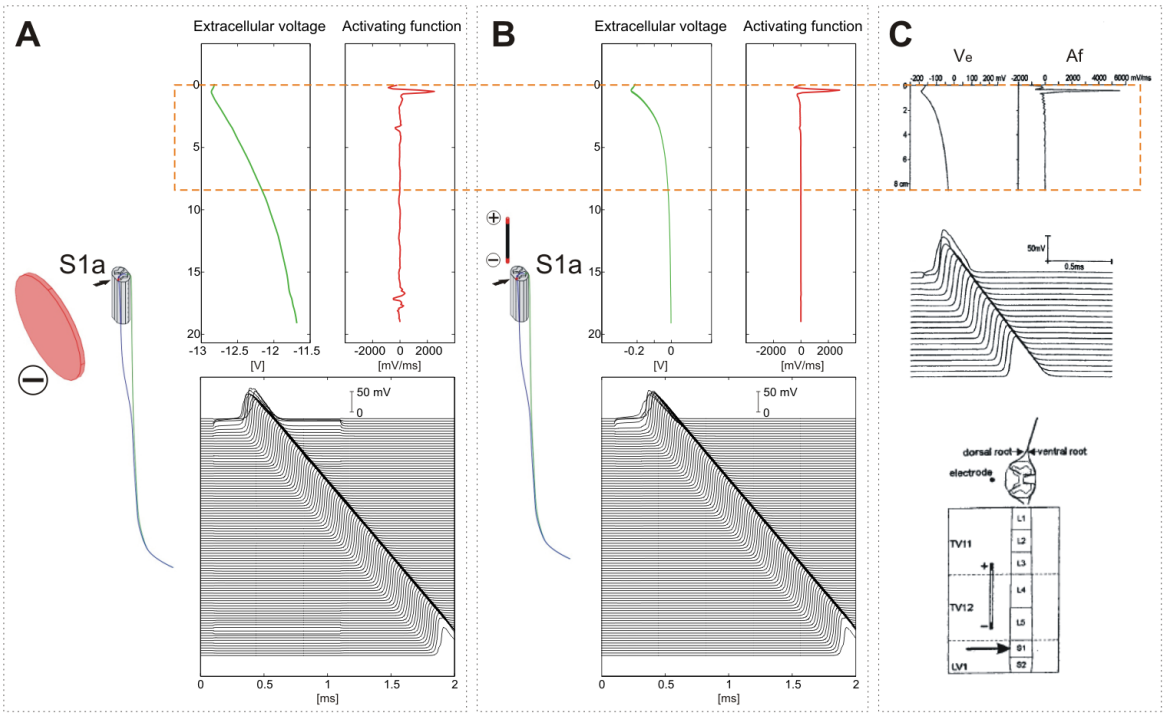

Figure 6.1.: Excitation of dorsal root fiber S1a in tSCS (A) and eSCS (B) in comparison with eSCS simulation results from [Rattay et al. 2000, Minassian 2000] (C).

6.2. Relationship between Stimulus Strength and Muscle Response

Transcutaneous electrical lumbar cord stimulation elicits individual twitches of the lower limb muscles when stimuli are delivered at low frequencies. The recruited muscle groups depend on the stimulus strength and the position of the electrodes [Minassian et al. 2007a].

Action potentials initiated in the large dorsal root fibers seem to pass directly to the motor neuron of the same spinal cord segment (monosynaptic pathway) [Rattay et al. 2000]. According to the segmental arrangement of muscle innervation, and considering the monosynaptic pathways (Section 2.4), the recruitment order of dorsal roots is directly related to the sequence of responses of corresponding muscle groups. The aim is to find a relation between stimulus strength and recruitment of dorsal root fibers entering different spinal cord segments.

In the simulations the excitable neural structures of the spinal cord are reduced to 15 target neurons. Five DR fibers and five VR fibers entering the lower spinal cord at equidistant levels are simulated plus five additional DR fibers which enter the lumbosacral cord at intermediate levels. Applying interpolation methods allows to predict the thresholds for roots which were not considered in the simulations.

Figure 6.2 presents the threshold voltages of nine DR fibers entering the spinal cord at different levels, marked by arrows in (A) and (B), and interpolated values for entry levels inbetween (C). The two models of spinal cord segment arrangement derived from the results of [Wall et al. 1990] and of [Lang and Geisel 1983], respectively, are shown in (A) and (B), including the innervation scheme of lower limb muscles (see Section 2.5). The grey levels in the shaded regions indicate the excitability of the 'segmental arrangement of innervation'. In (D) the results of the clinical observations are shown. White circles represent mean response thresholds of the muscles (quadriceps, hamstring, tibialis anterior, and triceps surae) as percentage of the common threshold intensity. Considering segmental arrangement model (A) in Figure 6.2 it is not possible to identify a muscle group with a significantly high or low stimulation threshold. According to model (B) dorsal root fibers entering segments 4 and 5 show a high threshold, which results in a high threshold for TA recruitment. This is in conformity with the the findings from [Minassian et al. 2007a] (D).

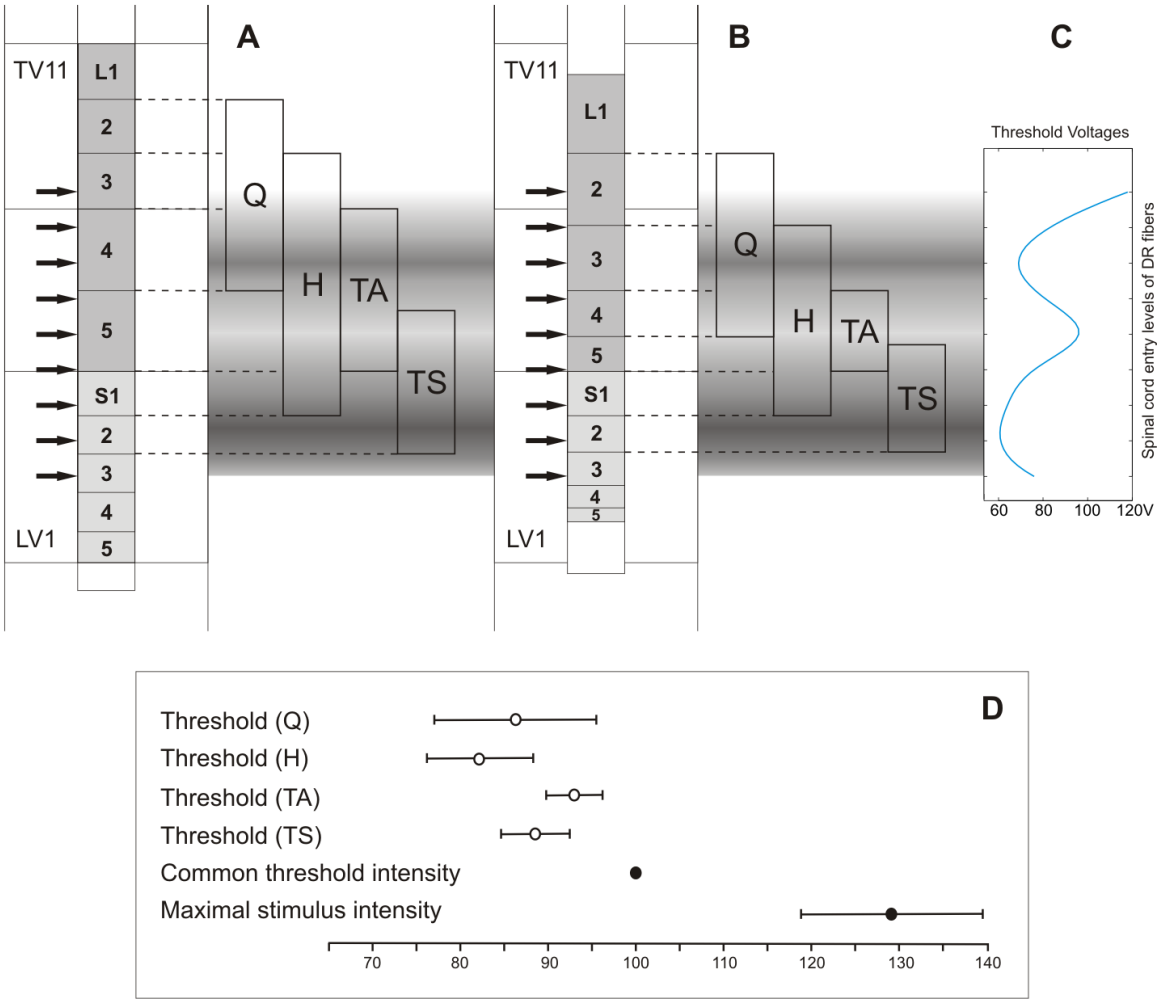

Figure 6.2.: Muscle recruitment in tSCS considering different segmental arrangements of innervation (A) and (B). Arrows mark the spinal cord entry levels of the simulated DR fibers. Excitation tresholds of DR fibers dependent on their cord entry level (C), and the results of muscle twitch measurements from [Minassian et al. 2007a] (D). Details described in the text.

In [Minassian et al. 2007a] the mean common threshold intensity needed to elicit reflexes bilaterally in all muscles was 28.6 ±6.3V in a seven-subject group, which is significantly lower than the threshold values calculated in the simulations for this study. Possible reasons are discussed in Section 6.3.

Dorsal column fibers were not simulated in this study because their excitation thresholds in tSCS are expected to be considerably higher compared to those of root fibers for two reasons: (i) The diameters of DC fibers are smaller than those of corresponding dorsal root fibers, and (ii) DC fibers do not show curvatures along their trajectories. Furthermore, the difference in thresholds for DC fibers and DR fibers has been demonstrated in case of eSCS [Minassian et al. 2007b, Minassian 2000].

Summarizing, the presented simulation results provide a biophysical explanation for the clinical observation of segmental-selective, stimulus strength dependent motor effects induced by transcutaneous lumbosacral cord stimulation as reported in [Minassian et al. 2007a]. The calculated relation between stimulus strength and recruitment order of dorsal root fibers entering different spinal cord segments closely resembles the relation identified by muscle twitch measurements.

6.3. Factors Limiting the Accuracy of the Simulations

The calculated excitation thresholds (Chapter 5) are clearly above the measured ones (Section 6.2, [Minassian et al. 2007a]). In the following sections the principal factors causing this discrepancy are discussed.

6.3.1. Skin Capacitance

In the simulations for this study the capacitive effects of body tissues are disregarded, since currents within the body have been shown to be primarily conduction currents [Schwan and Kay 1957]. The volume conductor is considered purely resistive (Chapter 3). However, in voltage regulated stimulation, as used in this simulation study and in electrophysiological measurements [Minassian et al. 2007a, Hofstoetter et al. 2008], the tissue resistivities and the permittivities - primarily the properties of the skin - directly influence nerve activation [Kuhn 2008].

Equivalent circuit models can be used to understand the basic effects when a voltage regulated source is used in transcutaneous electrical stimulation (TES). Figure 6.3 shows the voltages and currents that are present at the different resistors and capacitors. The voltage across the skin layer increases over time because of the high skin capacitance and thus the extracellular potentials along nerve fibers within the body drop during the course of the applied pulse, as displayed in (B). Using biphasic pulses the body voltage amplitude arrives at its maximum value at onset of the second pulse phase (C). This effect results in lower threshold values for the excitation of nerve fibers in voltage regulated transcutaneous stimulation.

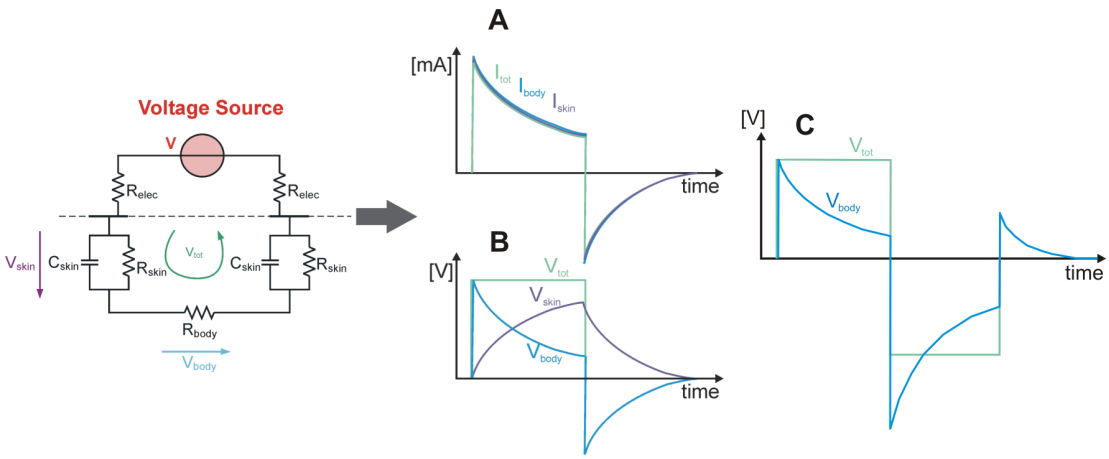

Figure 6.3.: Simple equivalent circuit model of transcutaneous electrical stimulation for voltage regulated pulses. Plots (A) and (B) depict the currents and voltages across the skin and body tissues for a rectangular voltage pulse. In (C) the change in voltage across the body for a symmetric biphasic pulse is shown. R_{elec} is assumed to be small compared to the other resistivities. After A. Kuhn, 2008.

6.3.2. Rheobase and Chronaxie

For assessment of the excitability of nerve fibers the rheobase and chronaxie are used as indicators. The rheobase is the minimal current amplitude of 'infinite' duration (practically, a few hundred milliseconds) that produces an AP. Chronaxie is the pulse duration required for fiber threshold with an amplitude of twice the rheobase. Both indicators can be derived from strength-duration curves, which describe the stimulation current amplitude versus the pulse duration for threshold activation, see Figure 6.4.

In [Kuhn 2008] strength-duration curves calculated using several nerve fiber models are compared with experimentally measured thresholds for different pulse durations. The results show that the rheobase calculated with the fiber model involving CRRSS membrane dynamics, as used in this study, is at least a factor of four higher than the experimentally obtained rheobase. The thresholds calculated with a more complex model incorporating a double cable structure developed by McIntyre et al. better match the measurements [McIntyre et al. 2002].

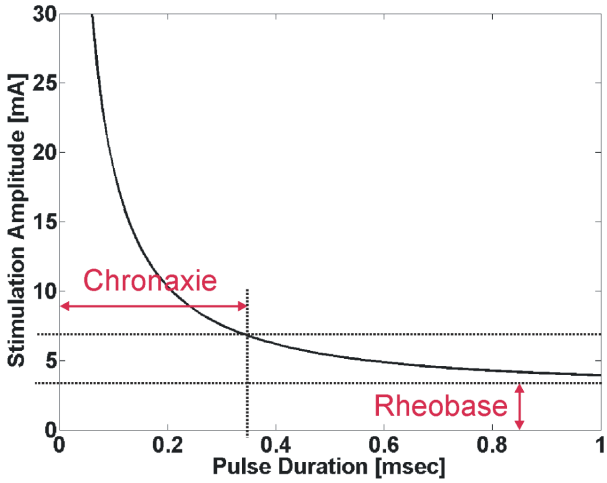

Figure 6.4.: Strength-Duration curve with rheobase and chronaxie indicated. After A. Kuhn, 2008.

6.3.3. Node Positions

The influence of the node positions on fiber threshold was investigated by shifting the nodes of several fibers in 0.2mm steps within the internodal distances. Changes in threshold voltage of up to 27% were observed. This can explain the difference in threshold values of the dorsal L2a and the ventral L2e fibers, both having their spike initiation sites in a region where the trajectories of the two fibers are almost identical. In general, the lowest threshold is obtained for a fiber if a node of Ranvier is located at the 'hot spot' of the fiber, where the extracellular voltage profile shows the strongest curvature. The effect of node positons on excitation thresholds has been considered in the comparison of dorsal root fiber excitability in Section 6.2. The nodes of the simulated DR fibers are located at comparable positions along the fiber pathways around their 'hot spots'.

6.3.4. VC Model Geometry

A well defined geometry of the volume conductor model is essential for the quality of the computations. A simplified finite element geometry was modeled to represent the complex anatomical structures. The dura mater, separating the cerebrospinal fluid from the epidural fat, and the small spinal root filaments, immersed in the well conducting fluid, were not modeled as separate compartments. This is valid under the assumption that the potential distribution in the region of interest is not affected by the presence of these thin tissues in tSCS.

7. Conclusion

A boundary value problem involving the Laplace equation is solved utilizing the finite element method to obtain the stimulation-induced electrical potentials in the biological system of the spinal cord and the surrounding anatomical structures. The excitation of spinal cord neurons caused by the electric field is simulated with a nerve fiber model considering the complex behavior of the neuronal membrane. The results of the computations inform about the excitability of the different neural elements when the lower spinal cord is stimulated with electrodes, from the surface or using implants.

The afferent fibers of the dorsal spinal roots with the largest diameters of $20\mu m$ have the lowest excitation thresholds. Stronger stimuli are required to excite even the thickest efferent neurons of the ventral roots.

For the spinal root fibers the initiation of action potentials is not restricted to their entry zone into the spinal cord for rather small stimulation strengths when stimulated from the surface. In this case spikes can be initiated in the region where the root fibers exit the spinal canal. These two potential excitation sites are each characterized by a strong curvature of the root fibers and a border between anatomical structures with significantly different conductivities.

Low thresholds are caused by strong curvatures of the extracellular voltage profiles along the fibers. For a given stimulus intensity the curvature of the extracellular voltage profile and thus the excitability of a spinal root fiber is mostly influenced by (i) the spinal cord entry level of the root fiber with respect to the spinous processes of the vertebrae, (ii) the curvature of the fiber, and (iii) the change of electrical conductivity at the entry of the root into the spinal cord and at its exit from the spinal canal.

Furthermore, excitation thresholds are affected by the stimulus pulse shape. Applying symmetric biphasic rectangular pulses lower thresholds are obtained compared to the use of monophasic rectangular pulses. The first phase has an advantageous effect on the starting condition of the initiation of an action potential by the second phase.

The results of the simulations provide a biophysical interpretation and explanation for the clinical observation of muscle responses in the lower limbs induced by spinal cord stimulation with surface electrodes. The calculated relation between stimulus strength and recruitment order of dorsal root fibers entering different spinal cord segments closely resembles the relation identified by muscle twitch measurements.

With appropriate positions for surface and implanted electrodes, similar excitation patterns of the same target neurons are obtained, both in experiment and in the simulation study, which results in a comparable neural input for the central pattern generators within the spinal cord. Thus, similar effects can be expected in both stimulation strategies.

A. Appendix

This appendix contains the code of a sample MATLAB program used to calculate the response behavior of a myelinated nerve fiber, i.e. membrane voltage along the fiber trajectory, and thereby its excitation threshold. The input is an array of electrical potential values calculated by the FEM and evaluated at numerous coordinates along the fiber pathway within the 3D volume conductor model. The output includes the extracellular voltage V_e as a function of the fiber length coordinate, the activating function and the membrane voltage at each node as a function of time.

A.1. MATLAB Code

The following m-file was written and executed in The Mathworks MATLAB version 7.6 (R2008a). Stimulation voltage, duration of the simulation and onset and offset of the stimulus pulse have to be specified. Parameters like fiber diameter and node length or the electrode polarity can easily be changed.

```
function crrss_compact(V_stim,T,stim_on,stim_off)
% V_stim: stimulation voltage [V]
% T: time [ms]

% parameters
% ------------------------------------------------------------------
l_n = 1.5e-4;          % node length [cm]
D = 20e-4;             % fiber diameter with myelin sheath [cm]
N_layers = 75e4*D;     % represents internodal myelin sheath
                       % (derived according to velocity check)
g_Na = 1445;           % sodium channel conductivity [mS/cm^2]
g_l = 128;             % leak channel conductivity [mS/cm^2]
V_Na = 115;            % Nernst potential for sodium channels [mV]
V_l = -0.01;           % Nernst potential for leakage channels [mV]
r = 0.07;              % specific resistivity [kOhm*cm]
```

```
c = 1;                  % specific capacity [m2uF/cm^2]
g = 1;                  % internodal membrane conductivity [mS/cm^2]
k = 1;                  % 37°C  k=3^(0.1*T-3.7)
V_fem = 50;             % Voltage applied in FEM simulation [V]
polarity = -1;          % -1/+1 ... neg./pos. active electrode
% ---------------------------------------------------------------

l_in = 100*D;
C_in = l_in * (0.64*D)*pi * c / N_layers;
C_n = l_n * (0.64*D)*pi * c;
R_in = 4*r * l_in /((0.64*D)^2*pi);
R_n = 4*r * l_n /((0.64*D)^2*pi);
g_m = l_in * (0.64*D)*pi * g / N_layers;
gNa_n = l_n * (0.64*D)*pi * g_Na;
gl_n = l_n * (0.64*D)*pi * g_l;

% read axon data file
% ---------------------------------------------------------------
reply = input('data file: ','s');
DATA = importdata(reply);
%DATA = DATA.data;      % for MATLAB_7 R14
Ve_pulse = -polarity*1000*DATA(:,4)*V_stim/V_fem;
x = 100*DATA(:,1);
y = 100*DATA(:,2);
z = 100*DATA(:,3);
% N_comp odd, nodes at both ends, calculated in fiber_compcoords_Ve.m
N_comp = length(x)-2;

% fiber length and interpolation to obtain Ve_pulse at the exact location
% along the fiber trajectory (longitudinal center of each compartment)
% (s and interp1 optional, but more accurate)
% ---------------------------------------------------------------
s(1) = -l_in/2;
for i=1:length(x)-1
    s(i+1) = s(i)+sqrt((x(i+1)-x(i))^2+(y(i+1)-y(i))^2+(z(i+1)-z(i))^2);
end

xi = zeros(N_comp+2,1);
xi(1) = -l_in/2;
% to investigate influence of node position:
% xi(1) = -l_in/2 + j*l_in/10;   % for j=1:10
for i=2:N_comp+2
    xi(i) = xi(i-1) + (l_n + l_in)/2;
end

Ve_pulse = interp1(s,Ve_pulse,xi,'linear','extrap');
```

```
disp ('fiber length [cm] =')
disp (s(length(x))-l_in/2)
disp ('N_comp =')
disp (N_comp)
% ---------------------------------------------------------------

% initial condition vector
% ---------------------------------------------------------------
IC = zeros (2*N_comp+3,1);
for i=N_comp+3:2:2*N_comp+2
    IC(i) = 0.003;
    IC(i+1) = 0.75;
end

% numerical solving
% ---------------------------------------------------------------
%tspan = 0:0.01:T;
[t,Y] = ode15s (@odesys, [0,T],IC);

% plotting
% ---------------------------------------------------------------
scrsz = get(0,'ScreenSize');
% plotting gating variables m,h (optional)
CH = zeros(length(t),N_comp+1);
for i=1:(N_comp+1)/2
    CH(:,i) = Y(:,N_comp+1+2*i) -3*(i-1)/10;
    CH(:,(N_comp+1)/2+i) = Y(:,N_comp+2+2*i) -3*((N_comp+5)/2+i)/10;
end

figure('Position',[scrsz(3)/3 40 scrsz(3)/2 5*scrsz(4)/6])
plot (t,CH,'DisplayName','CH');

V = zeros(length(t),(N_comp+1)/2);
for i=1:(N_comp+1)/2
    V(:,i) = Y(:,2*i) -6*(i-1);   % displacement
end

figure('Position',[5 40 scrsz(3)-10 5*scrsz(4)/6],'Name',...
    ['Stimulus: ' int2str(V_stim) 'V / ' int2str(stim_off-stim_on) ...
    'ms - Response of  ' reply '  (only nodes shown)'])
subplot(1,4,3:4);
plot(t,V,'k','DisplayName','V');
xlabel('[ms]','FontSize',14); %ylabel('V [mV]');
title('Membrane voltage','FontSize',14);
set(gca,'YAxisLocation','right','YTick',[],'YLim',...
```

```
    [-3*(N_comp-1)-50 100],'XTick',[0 0.5 1 1.5 2],'FontSize',14);

% ---------------------------------------------------------------

% method to find out propagation velocity
% and spike initiation compartments (optional)
if max(max(Y))>50
    count = 0;
    disp ('for propagation velocity in m/s:')
    disp (10000*D*6)
    disp ('number of peaks within 0.2 ms should be')
    disp (round(2400*D/(l_n+l_in)))
    [C,I] = max(Y);
    for i=1:length(C)
        if C(i)>50
            I(i)=I(i);
        else
            I(i)=length(t);
        end
        % propagation velocity only correct for ONE spike train
        % in the following interval
        if ((t(I(i)) ≥ stim_off+0.1) & (t(I(i)) ≤ stim_off+0.6))
            count = count+1;
        end
    end
    [C,init] = sort(I);
    title(['first 3 spikes at compartments: ' int2str(init(1)-1) ...
         ',' int2str(init(2)-1) ',' int2str(init(3)-1)]);
    disp('propagation velocity in m/s:')
    disp(10*count*(l_n+l_in))
end

% subfunction: ode system
% ---------------------------------------------------------------
    function dY = odesys (t,Y)

    dY = zeros (2*N_comp+3,1);
    V_e = zeros (N_comp+2,1);

    alpha_m = zeros (N_comp+1,1);
    beta_m = zeros (N_comp+1,1);
    alpha_h = zeros (N_comp+1,1);
    beta_h = zeros (N_comp+1,1);

    % stimulus between stim_on and stim_off ms
    if t≥stim_on
```

```
        if t≤stim_off
            V_e = Ve_pulse;
        end
    end

    % symmetric biphasic stimulus with pulse width stim_off−stim_on ms
    %if (t≥stim_on) && (t≤(stim_on+stim_off)/2)
    %    V_e = −Ve_pulse;
    %end
    %if (t>(stim_on+stim_off)/2) && (t≤stim_off)
    %    V_e = Ve_pulse;
    %end

    % nodes
    for i=2:2:N_comp+1
        alpha_m(i) = (97 + 0.363*Y(i)) / (1 + exp((31 − Y(i))/5.3));
        beta_m(i) = alpha_m(i) / exp((Y(i) − 23.8)/4.17);
        beta_h(i) = 15.6 / (1 + exp((24 − Y(i))/10));
        alpha_h(i) = beta_h(i) / exp((Y(i) − 5.5)/5);

        dY(i) = (−(gNa_n * Y(N_comp+i+1)^2 * Y(N_comp+i+2) * (Y(i)−V_Na)...
                + gl_n * (Y(i)−V_l)) + 2*(Y(i−1)−Y(i))/(R_in + R_n) + ...
                2*(Y(i+1)−Y(i))/(R_in + R_n) + ...
                2*(V_e(i−1)−V_e(i))/(R_in + R_n) + ...
                2*(V_e(i+1)−V_e(i))/(R_in + R_n) )/C_n;
        dY(N_comp+i+1) = (−(alpha_m(i) + beta_m(i)) ...
                        * Y(N_comp+i+1) + alpha_m(i)) *k;
        dY(N_comp+i+2) = (−(alpha_h(i) + beta_h(i)) ...
                        * Y(N_comp+i+2) + alpha_h(i)) *k;

        act_fn(i−1) = (2*(Ve_pulse(i−1)−Ve_pulse(i))/(R_in + R_n) + ...
                      2*(Ve_pulse(i+1)−Ve_pulse(i))/(R_in + R_n))/C_n;
    end

    % internodes
    for i=3:2:N_comp
        dY(i) = (−g_m * Y(i) + 2*(Y(i−1)−Y(i))/(R_in + R_n) + ...
                2*(Y(i+1)−Y(i))/(R_in + R_n) + ...
                2*(V_e(i−1)−V_e(i))/(R_in + R_n) + ...
                2*(V_e(i+1)−V_e(i))/(R_in + R_n) )/C_in;

        act_fn(i−1) = (2*(Ve_pulse(i−1)−Ve_pulse(i))/(R_in + R_n) + ...
                      2*(Ve_pulse(i+1)−Ve_pulse(i))/(R_in + R_n))/C_in;
    end
    end
% ————————————————————————————————————————————————————————————————————————
```

```
% plotting continued
% ------------------------------------------------------------------
% plot Ve_pulse & activating function along the fiber

subplot(1,4,1);
plot(Ve_pulse/1000,xi, 'Color',[0 .75 0]);
xlabel('[V]','FontSize',14);
ylabel('Distance along fiber [cm]','FontSize',14);
hold off
axis ij
% for alignment with membrane voltage plot
factor = (xi(N_comp+2)-l_in/2)/(3*(N_comp-1));
set(gca,'YTick',[0 5 10 15 20],'FontSize',14);
%set(gca,'XLim',[limits]);
set(gca,'YLim',[-100*factor (xi(N_comp+2)-l_in/2)+50*factor]);
title('Extracellular voltage');

subplot(1,4,2);
plot(act_fn,xi(2:N_comp+1), 'Color',[.95 0 0]);
xlabel('[mV/ms]','FontSize',14);
axis ij
set(gca,'YTick',[0 5 10 15 20],'YTickLabel',{},'YLim',...
    [-100*factor (xi(N_comp+2)-l_in/2)+50*factor]);
set(gca,'XTick',[-2000 0 2000],'XLim',[-4000 4000],'FontSize',14);
title('Activating function');
end
```

Bibliography

A.G. Brown. *Organization in the Spinal Cord. The Anatomy and Physiology of Identified Neurons*. Springer-Verlag, Berlin, 1981. (Cited on pages 10, 12, 13, 14, and 32.)

S.Y. Chiu, J.M. Ritchie, R.B. Rogart, and D. Stagg. A quantitative description of membrane currents in rabbit myelinated nerve. *J. Physiol.*, 292:149 – 166, 1979. (Cited on pages 3 and 27.)

B. Coburn and W.K. Sin. A theoretical study of epidural electrical stimulation of the spinal cord - Part I: Finite element analysis of stimulus fields. *IEEE Trans. Biomed. Eng.*, 32(11):971 – 977, 1985. (Cited on pages 22 and 23.)

M.S. Cohen, E.J. Wall, C.W. Kerber, J.J. Abitbol, and S.R. Garfin. Organization of intrathecal nerve roots at the level of the conus medullaris. *J. Bone. Joint. Surg. [Br]*, 73(3):381 – 384, 1991. (Cited on pages 12 and 33.)

J.E. Desmedt and G. Cheron. Central somatosensory conduction in man: Neural generators and interpeak latencies of the far field components recorded from neck and right or left scalp and ear lobes. *Electroencephalgr. Clin. Neurophysiol.*, 50:382 – 403, 1980. (Cited on page 14.)

M.R. Dimitrijevic, Y. Gerasimenko, and M.M. Pinter. Evidence for a spinal central pattern generator in humans. *Ann. N.Y. Acad. Sci.*, 860:360 – 376, 1998. (Cited on page 1.)

K. R. Foster and H. P. Schwan. Dielectric properties of tissues and biological materials: a critical review. *Crit. Rev. Biomed. Eng.*, 17(1):25 – 104, 1989. (Cited on pages 22, 23, 45, and 46.)

R.E.W. Fyffe. *Handbook of the Spinal Cord Vols. 2 & 3. Anatomy and Physiology*, chapter Afferent fibers. Dekker, New York, 1984. (Cited on page 13.)

S. Gabriel, R. W. Lau, and C. Gabriel. The dielectric properties of biological tissues: III. parametric models for the dielectric spectrum of tissues. *Phys. Med. Biol.*, 41(11):2271 – 2293, 1996. (Cited on pages 23, 45, and 46.)

L.A. Geddes and L.E. Baker. The specific resistance of biological material - A compendium of data for the biomedical engineer and physiologist. *Med. Biol. Eng.*, 5: 271 – 293, 1967. (Cited on page 23.)

W.Y. Gu, M.A. Justiz, and H. Yao. Electrical conductivity of lumbar anulus fibrosis: effects of porosity and fixed charge density. *Spine*, 27(21):2390 – 2395, 2002. (Cited on page 23.)

T. Hasegawa, Y. Mikawa, R. Watanabe, and H.S. An. Morphometric analysis of the lumbosacral nerve roots and dorsal root ganglia by magnetic resonance imaging. *Spine*, 21(9):1005 – 1009, 1996. (Cited on pages 12 and 33.)

U.S. Hofstoetter, K. Minassian, C. Hofer, W. Mayr, F. Rattay, and M.R. Dimitrijevic. Modification of reflex responses to lumbar posterior root stimulation by motor tasks in healthy subjects. *Artif. Organs*, 32(8):644 – 648, 2008. (Cited on pages 1, 20, 35, 41, 59, and 63.)

J. Holsheimer. Computer modelling of spinal cord stimulation and its contribution to therapeutic efficacy. *Spinal Cord*, 36:531 – 540, 1998. (Cited on pages 1, 11, 22, and 23.)

T. Hongo, N. Kudo, S. Sasaki, M. Yamashita, K. Yoshida, N. Ishizuka, and H. Mannen. Trajectory of Group Ia and Ib fibers from the hind-limb muscles at the L3 and L4 segments of the spinal cord of the cat. *J. Compar. Neurol.*, 262:159 – 194, 1987. (Cited on page 14.)

J.B. Hursh. Conduction velocity and the diameter of nerve fibers. *Am. J. Physiol.*, 127(1):131 – 139, 1939. (Cited on pages 14 and 28.)

C.R. Johnson. Computational and numerical methods for bioelectric field problems. *Crit. Rev. Biomed. Eng.*, 25:1 – 81, 1997. (Cited on page 17.)

E.R. Kandel, J.H. Schwartz, and T.M. Jessell. *Principles of Neural Science*. McGraw-Hill, New York, fourth edition, 2000. (Cited on pages 5 and 7.)

R.N. Klepfer, C.R. Johnson, and R.S. Macleod. The effects of inhomogeneities and anisotropies on electrocardiographic fields: A 3-D finite-element study. *IEEE Trans. Biomed. Eng.*, 44(8):706 – 719, 1997. (Cited on pages 15 and 46.)

A. Kuhn. *Modeling transcutaneous electrical stimulation.* Phd thesis (dissertation), ETH Zurich, 2008. (Cited on pages 23, 63, and 65.)

J. Lang. *Neuroorthopädie 2*, chapter Lendenwirbelsäulenerkrankungen mit Beteiligung des Nervensystems. Springer, Berlin, 1984. (Cited on pages 10, 12, 33, and 38.)

J. Lang and Geisel. Über den lumbosakralen Teil des Durasackes und die Topographie seines Inhalts. *Morphol. Med.*, 3:27 – 46, 1983. (Cited on pages 13, 35, and 61.)

J. Malmivuo and R. Plonsey. *Bioelectromagnetism: Principles and Applications of Bioelectric and Biomagnetic Fields.* Oxford University Press, New York, first edition, 1995. (Cited on pages 22 and 23.)

C.C. McIntyre, A.G. Richardson, and W.M. Grill. Modeling the excitability of mammalian nerve fibers: Influence of afterpotentials on the recovery cycle. *J. Neurophysiol.*, 87:995 – 1006, 2002. (Cited on page 65.)

D.R. McNeal. Analysis of a model for excitation of myelinated nerve. *IEEE Trans. Biomed. Eng.*, 23(4):329 – 337, 1976. (Cited on page 26.)

D. Miklavcic, N. Pavselj, and F.X. Hart. Electric Properties of Tissues. In *Wiley Encyclopedia of Biomedical Engineering.* John Wiley & Sons, New York, 2006. (Cited on pages 22, 23, 45, and 46.)

K. Minassian. Excitation of lower spinal cord structures with implanted electrodes: 3d finite element analysis and simulation of neural responses. Master's thesis (diplomarbeit), Vienna University of Technology, 2000. (Cited on pages 11, 13, 35, 49, 56, 60, and 63.)

K. Minassian, B. Jilge, F. Rattay, M.M. Pinter, H. Binder, F. Gerstenbrand, and M.R. Dimitrijevic. Stepping-like movements in humans with complete spinal cord injury induced by epidural stimulation of the lumbar cord: Electromyographic study of compound muscle action potentials. *Spinal Cord*, 42:401 – 416, 2000. (Cited on page 1.)

K. Minassian, I. Persy, F. Rattay, M.R. Dimitrijevic, C. Hofer, and H. Kern. Posterior root-muscle reflexes elicited by transcutaneous stimulation of the human lumbosacral cord. *Muscle & Nerve*, 35:327 – 336, 2007a. (Cited on pages 1, 20, 35, 41, 59, 61, 62, and 63.)

K. Minassian, I. Persy, F. Rattay, M.M. Pinter, H. Kern, and M.R. Dimitrijevic. Human lumbar cord circuitries can be activated by extrinsic tonic input to generate locomotor-like activity. *Human Movement Science*, 26:275 – 295, 2007b. (Cited on pages 1, 59, and 63.)

M. Murg, H. Binder, and M.R. Dimitrijevic. Epidural electric stimulation of posterior structures of the human lumbar spinal cord: 1. muscle twitches - a functional method to define the site of stimulation. *Spinal Cord*, 38(7):394 – 402, 2000. (Cited on pages 1 and 59.)

M.M. Pinter, F. Gerstenbrand, and M.R. Dimitrijevic. Epidural electrical stimulation of posterior structures of the human lumbosacral cord: 3. Control Of spasticity. *Spinal Cord*, 38(9):524 – 531, 2000. (Cited on page 59.)

V. Raicu, N. Kitagawa, and A. Irimajiri. A quantitative approach to the dielectric properties of the skin. *Phys. Med. Biol.*, 45:L1 – L4, 2000. (Cited on page 23.)

F. Rattay. Modelling of the excitation and the propagation of nerve impulses by natural and artificial stimulations. *Math. Comput. Simul.*, 39:589 – 595, 1995. (Cited on page 27.)

F. Rattay. Analysis of the electric excitation of CNS neurons. *IEEE Trans. Biomed. Eng.*, 45(6):766 – 772, 1998. (Cited on pages 7 and 26.)

F. Rattay. The basic mechanism for electrical stimulation of the nervous system. *Neuroscience*, 89(2):335 – 346, 1999. (Cited on pages 7, 26, 28, 29, and 32.)

F. Rattay, K. Minassian, and M.R. Dimitrijevic. Epidural electrical stimulation of posterior structures of the human lumbosacral cord: 2. quantitative analysis by computer modeling. *Spinal Cord*, 38:473 – 489, 2000. (Cited on pages 1, 11, 13, 22, 23, 32, 35, 49, 51, 56, 59, 60, and 61.)

H.P. Schwan and C.F. Kay. Capacitive properties of body tissues. *Circ. Res.*, 5(4): 439 – 443, 1957. (Cited on pages 16 and 63.)

M.C. Smith and P. Deacon. Topographical analysis of the posterior columns of the spinal cord in man. The long ascending fibres. *Brain*, 107:671 – 698, 1984. (Cited on pages 12 and 13.)

J.J. Struijk, J. Holsheimer, B.K. van Veen, and H.B.K. Boom. Epidural spinal cord stimulation: calculation of field potentials with special reference to dorsal column nerve fibers. *IEEE Trans. Biomed. Eng.*, 38(1):104 – 110, 1991. (Cited on pages 22 and 23.)

J.J. Struijk, J. Holsheimer, G.G. van der Heide, and H.B.K. Boom. Recruitment of dorsal column fibers in spinal cord stimulation: influence of collateral branching. *IEEE Trans. Biomed. Eng.*, 39(9):903 – 912, 1992. (Cited on pages 22, 23, and 32.)

J.J. Struijk, J. Holsheimer, G. Barolat, J. He, and H.B.K. Boom. Paresthesia thresholds in spinal cord stimulation: A comparison of theoretical results with clinical data. *IEEE Trans. Rehab. Eng.*, 1(2):101 – 108, 1993a. (Cited on pages 1, 22, and 23.)

J.J. Struijk, J. Holsheimer, and H.B.K. Boom. Excitation of dorsal root fibers in spinal cord stimulation: A theoretical study. *IEEE Trans. Biomed. Eng.*, 40(7):632 – 639, 1993b. (Cited on page 59.)

J.D. Sweeney, J.T. Mortimer, and D. Durand. Modeling of mammalian myelinated nerve for functional neuromuscular electrostimulation. In *Proc. 9th Ann. Conf. IEEE EMBS*, pages 1577 – 1578, 1987. (Cited on pages 3, 27, 30, and 32.)

Z. Szava. Three-dimensional finite element simulation of the electrical field distribution within the vertebral canal generated by surface electrodes. Master's thesis (diplomarbeit), University of Applied Sciences Technikum Wien, 2006. (Cited on pages 2, 20, 22, and 23.)

E.J. Wall, M.S. Cohen, J.J. Abitbol, and S.R. Garfin. Organization of intrathecal nerve roots at the level of the conus medullaris. *J. Bone. Joint. Surg. [Am]*, 72(10): 1495 – 1499, 1990. (Cited on pages 12, 13, 33, 35, and 61.)